







Research Article

The Pantheon+ analysis: Improving the redshifts and peculiar velocities of Type Ia supernovae used in cosmological analyses

Anthony Carr¹, Tamara M. Davis¹, Dan Scolnic², Khaled Said¹, Dillon Brout³, Erik R. Peterson², and Richard Kessler^{4,5}

¹School of Mathematics and Physics, University of Queensland, Brisbane, QLD 4072, Australia, ²Department of Physics, Duke University, Durham, NC 27708, USA, ³Center for Astrophysics, Harvard & Smithsonian, 60 Garden Street, Cambridge, MA 02138, USA, ⁴Kavli Institute for Cosmological Physics, University of Chicago, Chicago, IL 60637, USA and ⁵Department of Astronomy and Astrophysics, University of Chicago, Chicago, IL 60637, USA

Abstract

We examine the redshifts of a comprehensive set of published Type Ia supernovae, and provide a combined, improved catalogue with updated redshifts. We improve on the original catalogues by using the most up-to-date heliocentric redshift data available; ensuring all redshifts have uncertainty estimates; using the exact formulae to convert heliocentric redshifts into the Cosmic Microwave Background (CMB) frame; and utilising an improved peculiar velocity model that calculates local motions in redshift-space and more realistically accounts for the external bulk flow at high-redshifts. We review 2607 supernova redshifts; 2285 are from unique supernovae and 322 are from repeat-observations of the same supernova. In total, we updated 990 unique heliocentric redshifts, and found 5 cases of missing or incorrect heliocentric corrections, 44 incorrect or missing supernova coordinates, 230 missing heliocentric or CMB frame redshifts, and 1200 missing redshift uncertainties. The absolute corrections range between $10^{-8} \leq \Delta z \leq 0.038$, and $\text{RMS}(\Delta z) \sim 3 \times 10^{-3}$. The sign of the correction was essentially random, so the mean and median corrections are small: 4×10^{-4} and 4×10^{-6} respectively. We examine the impact of these improvements for H_0 and the dark energy equation of state w and find that the cosmological results change by $\Delta H_0 = -0.12 \text{ km s}^{-1} \text{ Mpc}^{-1}$ and $\Delta w = 0.003$, both significantly smaller than previously reported uncertainties for H_0 of $1.0 \text{ km s}^{-1} \text{ Mpc}^{-1}$ and w of 0.04 respectively.

keywords: cosmology: theory – galaxies: distances and redshifts

(Received 26 May 2022; revised 5 August 2022; accepted 29 August 2022)

1. Introduction

The power of Type Ia Supernovae (SNe Ia) as a probe of the expansion history of the universe comes from comparing the measured distances of the SNe to the distances expected for their redshift in different cosmological models (Riess et al. 1998; Perlmutter et al. 1999; Wood-Vasey et al. 2007; Kessler et al. 2009; Betoule et al. 2014; Scolnic et al. 2018; Dark Energy Survey 2019). Since the relative precision of spectroscopically measured redshifts is typically significantly greater than that of redshift-independent distances, much more effort has been spent on improving distance measurements than improving redshift measurements (e.g. Phillips 1993; Phillips et al. 1999; Goldhaber et al. 2001; Guy et al. 2007; Jha, Riess, & Kirshner 2007; Hicken et al. 2009; Kessler et al. 2009; Scolnic et al. 2015; Kessler & Scolnic 2017; Brout et al. 2019; Kessler et al. 2019; Lasker et al. 2019). This prioritisation is supported by the fact that redshift measurements, either from the host galaxies or SNe, are straightforward; small errors are usually expected to be random, shifting redshifts higher as often as lower. However, with samples of greater than 1000 SNe, systematic uncertainties are of paramount concern, and potential systematic biases in the redshift measurements must be considered

(e.g. Huterer et al. 2004; Wojtak et al. 2015; Davis et al. 2019; Steinhardt, Sneppen, & Sen 2020; Mitra & Linder 2021). In this analysis, we perform a comprehensive review of the redshifts of individual SNe used in the latest samples for cosmological analyses and analyse potential biases due to issues with redshifts in the recovery of cosmological parameters.

Several recent papers have considered the impact of redshift errors on supernova cosmology. For example, Steinhardt et al. (2020) determined whether the source for each redshift in the Pantheon sample (Scolnic et al. 2018) was either the host galaxy spectrum or SN spectrum, and found difference in cosmological parameters at a $\sim 3\sigma$ level between the two subsets. Rameez & Sarkar (2021) noted changes in the measured redshifts of sub-samples of large SN compilations that were larger than the reported uncertainties and questioned the repeatability of SN experiments. While here we show the effect of redshift errors on cosmological parameters remains small (relative to their current precision), we note that the redshifts came from a variety of sources, with many measurements having been over 20 yr ago. Old and/or inhomogeneous redshift measurements are not necessarily a problem, but these factors increase the potential for miscellaneous errors to be carried through different SN samples, so a comprehensive review is warranted. Achieving accurate redshifts for cosmological studies requires multiple stages, and in this paper we apply improvements at each stage except for performing new spectroscopic measurements.

Corresponding author: Anthony Carr, Email: anthony.carr@uq.net.au

Cite this article: Carr A, Davis TM, Scolnic D, Said K, Brout D, Peterson ER and Kessler-R. (2022) The Pantheon+ analysis: Improving the redshifts and peculiar velocities of Type Ia supernovae used in cosmological analyses. *Publications of the Astronomical Society of Australia* 39, e046, 1–23. <https://doi.org/10.1017/pasa.2022.41>

Redshifts in the heliocentric frame are measured either from the SN spectrum, which is typically precise on the level of $\sigma_z \sim 0.005$ (a somewhat conservative estimation), or the host-galaxy spectrum, which is typically precise on the level of $\sigma_z \sim 0.0002$ (see Section 4). Host redshifts are preferred because the hosts have sharper spectral lines that result in a more accurate and precise redshift. However, it is essential for the correct host-galaxy to be associated with the SN (Gupta *et al.* 2016), else SNe will be misplaced on the Hubble diagram. Here we review the host galaxy assignment of all SNe where possible, and update heliocentric redshifts accordingly.

Once the heliocentric redshift is determined, we convert the redshift into the CMB frame. While the CMB conversion is standard, an unnecessary approximation has often been applied (see, e.g. Carr & Davis 2021, and references therein) and we replace that with the exact correction (Section 5).

The final step to obtain accurate cosmological redshifts is applying the correction to account for the peculiar velocity of the source. We introduce a slightly improved technique of estimating peculiar velocities (that also better models the external bulk flow to arbitrary redshift) based on the existing 2M++ compilation (Carrick *et al.* 2015). We apply this correction to all redshifts whereas previously, corrections had been applied only at low redshift, or with a biased model at large redshifts.

We thus release a comprehensive update to the redshifts of all publicly available Type Ia supernovae that make up the ‘Pantheon+’ sample. Unlike previous analyses, we do not isolate our work to redshifts of ‘cosmologically useful’ SNe (those that make it onto the Hubble diagram) since data cuts may be relaxed or otherwise altered in future analyses.

This paper is one of many that contribute to the Pantheon+ sample, culminating in the full cosmology analysis in Brout *et al.* (2022). This work is companion to Peterson *et al.* (2021), that studies the effects of replacing host galaxy redshifts with average redshifts of host galaxy groups on Hubble diagram residuals, and provides group-averaged redshifts and group-centre coordinates which we also release here. In addition, Peterson *et al.* (2021) studies the efficacy of using different peculiar velocity samples—including those derived in this work—on Hubble residuals. Brout *et al.* (2021) re-calibrates the many photometric systems of Pantheon+ and quantifies the systematic effects of photometric calibration on cosmological parameters. Scolnic *et al.* (2021) releases the 1701 updated light curves of 1550 unique SNe Ia^a used in the Pantheon+ *w* analysis and Supernovae and H0 for the Equation of State of dark energy (SH0ES) H_0 analysis (Riess *et al.* 2022). Peterson *et al.* (2021), Scolnic *et al.* (2021) and Brout *et al.* (2021, 2022) utilise the redshifts of this work, and we utilise the group-averaged redshifts from Peterson *et al.* (2021) and distance moduli from Brout *et al.* (2022) in our analysis of the effects of the redshift updates. See <https://PantheonPlusSH0ES.github.io> for the other papers that contribute to Pantheon+.

In this work, the main improvements we implemented are detailed in the following sections:

- Fixed coordinates and miscellaneous bookkeeping redshift errors (Section 2).
- Updated heliocentric redshift values using the NASA/IPAC Extragalactic Database (NED) when better redshifts were available (Section 3).

^aThe cosmology sample of this work differs in number to the full analysis due to our simplified data cuts and lack of full covariance analysis.

- Ensured all redshifts have uncertainty estimates (Section 4).
- Used the exact redshift conversion when (a) going from heliocentric redshifts to the CMB frame, and (b) going from CMB frame to Hubble diagram redshift (Section 5). These respectively correct for (a) our Sun’s motion with respect to the CMB and (b) the host galaxy’s motion with respect to the CMB.
- Provided improved peculiar velocity estimates that better represent the bulk flow at large distances (Section 6).

Next, we analyse the impact of each change on cosmological parameters in Section 7 and finally discuss and conclude in Section 8.

The Pantheon+ redshifts and accompanying data will be released as a machine readable Centre de Données astronomiques de Strasbourg (CDS) VizieR table with the publication of this work, and also on GitHub at <https://github.com/PantheonPlusSH0ES/DataRelease> which will log any possible updates. The light curves for each SN (see Scolnic *et al.* 2021), which contain our updated redshifts and peculiar velocities, are also available at this GitHub. The peculiar velocity method developed for this paper is available at <https://github.com/KSaid-1/pvhub>.

2. Samples and bookkeeping

Our aim is to complete a comprehensive review of the redshifts assigned to every publicly available SN Ia used for cosmology and other SN Ia studies. We include primarily normal Type Ia supernovae along with various Ia subtypes, such as ‘1991T-like’ or just ‘peculiar’ (Li *et al.* 2001). The Pantheon+ sample is compiled of supernovae taken from a diverse array of samples, as listed in Table 1 and shown in Figure 1. The master list of our updated redshifts, which includes the SN and host coordinates; heliocentric, CMB, and cosmological (Hubble diagram) redshifts; and peculiar velocity values, can be found in Table 2. Including all of these quantities aids in the traceability of the redshifts (and hosts) and repeatability of the corrections.

2.1 Description of parameters

The relevant parameters for our study are the redshifts and peculiar velocities. The heliocentric redshift (z_{hel}) is the ‘observed’ redshift.^b We convert from z_{hel} to the CMB frame redshift (z_{CMB}) using the standard formulae in Section 5 and emphasise that we do not approximate these transformations. CMB-frame redshift refers to the redshift after we correct for only *our own* peculiar velocity, that is we correct for the Planck-observed CMB dipole. The peculiar velocity (v_p) and corresponding peculiar redshift (z_p) refer to the motion of the distant galaxy that is in addition to the Hubble flow. The final Hubble-diagram redshift that is used for cosmology (z_{HD}) is the final stage, after we have corrected z_{CMB} for the peculiar velocity of the distant galaxy. The standard formulae are also given in Section 5, and the derivation of the peculiar velocities themselves is described in Section 6. Each of these parameters have uncertainties represented by σ . When the parameters come from the host galaxy group (from Peterson *et al.* 2021) instead of the individual host or SN, the symbol is preceded by ‘Group’.

^bHeliocentric redshifts are not quite the observed redshift, but we assume corrections for the Earth’s motion relative to the sun have been made correctly by the analysis software. This correction is small ($\Delta z \lesssim 10^{-6}$), so its effect would be negligible for current cosmological studies.

Table 1. Description of sub-samples and list of changes. N_{Tot} is the number of Type Ia (including subtypes) supernova light curves in each sample. See Section 3 for the definition of ‘best NED redshift’. See dot points in Sections 2.2 and 3 for more detailed descriptions of the improvements.

Source	Abbrev.	Ref.	N_{Tot}	z_{hel} range	Improvements
Hubble Deep Field North (using HST)	HDFN	1, 2	1	1.755	Corrected z_{hel} being listed as z_{CMB}
Supernova Cosmology Project (using HST)	SCP	3	8	1.014–1.415	Corrected z_{hel} being listed as z_{CMB} . Added coordinates. Reassigned uncertainties based on host or SN redshift
Cosmic Assembly Near Infra-Red Deep Extragalactic Legacy Survey and Cluster Lensing And Supernova survey with Hubble (using HST)	CANDELS+CLASH	4	13	1.03–2.26	Corrected z_{hel} being listed as z_{CMB} . Updated several z_{hel} to originally published values. Updated name and coordinates of one SN ^a
Complete Nearby (Redshift < 0.02) Sample of Type Ia Supernova Light Curves	CNIa0.02	5	17	0.0041–0.0303	Found best NED z_{hel} or added uncertainties where necessary
Center for Astrophysics (1)	CfA1	6	22	0.0031–0.123	Corrected coordinates of one SN. Found best NED z_{hel} . Added uncertainties. Identified hosts
Calán/Tololo survey	CTS	7	29	0.0104–0.101	Found best NED z_{hel} . Added uncertainties. Identified hosts
Great Observatories Origins Deep Survey and Probing Acceleration Now with Supernova (using HST)	GOODS+PANS	8, 9	29	0.457–1.390	Corrected z_{hel} being listed as z_{CMB} . Added coordinates. Reassigned uncertainties based on host or SN redshift
Center for Astrophysics (2)	CfA2	10	44	0.0067–0.0542	Found best NED z_{hel} . Added uncertainties. Identified hosts
Low-redshift (various sources)	LOWZ	11–23	66	0.0014–0.038	Found best NED z_{hel} . Added uncertainties. Identified hosts
Lick Observatory Supernova Search (2005–2018)	LOSS2	24	78	0.0008–0.082	Found best NED z_{hel} . Added uncertainties where necessary. Identified hosts
Center for Astrophysics (4p1, 4p2)	CfA4	25	94	0.0067–0.0745	Corrected coordinates of one SN. Found best NED z_{hel} . Added uncertainties. Identified hosts
Swift Optical/Ultraviolet Supernova Archive	SOUASA	26, 27	121	0.0008–0.0616	Found best NED z_{hel} . Added uncertainties. Identified hosts
Carnegie Supernova Project (DR3)	CSP	28	134	0.0038–0.0836	Found best NED z_{hel} . Added uncertainties. Identified hosts
Lick Observatory Supernova Search (1998–2008)	LOSS1	29	165	0.0020–0.0948	Found best NED z_{hel} . Added uncertainties. Identified hosts
Center for Astrophysics (3S, 3K)	CfA3	30	185	0.0032–0.084	Found best NED z_{hel} . Added uncertainties. Identified hosts
SuperNova Legacy Survey	SNLS	31	239	0.1245–1.06	Identified 10 hosts and updated those redshifts. Added uncertainties
Foundation Supernova Survey	FSS	32, 33	242	0.0045–0.1106	Corrected coordinates of six SNe. Updated one redshift ^b
Dark Energy Survey (3YR)	DES	34, 35	251 ^c	0.0176–0.850	Updated redshifts and reassigned uncertainties based on host or SN redshift. One additional redshift update ^d
Panoramic Survey Telescope & Rapid Response System Medium Deep Survey	PS1MD	36	370	0.0252–0.670	Identified 20 hosts and updated those redshifts. Updated one additional redshift ^e
Sloan Digital Sky Survey	SDSS	37	499 ^f	0.0130–0.5540	Identified hosts. Updated 127 redshifts

^aSNID vespasion: Pantheon ID was previously ‘vespesian’ (spelled with an e), and coordinates were mistakenly those of the supernova Obama (EGS110ba) (Riess et al. 2018). See new coordinates in Table 3.

^bPSNJ1628383 from FSS shares the same host group as SN 2009eu. See entry in Table A2.

^cThe DES sample contains 26 non-confirmed but highly probable SNe Ia spectroscopic classifications (type ‘SNIa?’ in Table 6 of Smith et al. 2020a). Of these, 22 pass our cosmology sample quality cuts.

^dUpdated with new OzDES redshifts and improved SN host association (M. Smith, private communication). The redshift of DES supernova 1280201 (DES15X3iv) was updated to the higher precision FSS measurement (ASASSN-15od).

^eThe PS1MD redshift of 580104 was updated to the higher precision DES measurement (1261579; DES13X3woy).

^fWe include only secure spectroscopic Type Ia classifications from SDSS, which excludes 41 SNe (type ‘SNIa?’ in Table 2 of Sako et al. 2018), four of which were originally in Pantheon (2005gv, 2005kt, 2007oq, 2007ow) cf. 22/26 DES ‘SNIa?’ in our cosmology sample, implying the SDSS SNIa? are less secure. A further two SNe (2006lo, 2006md) in Pantheon were excluded due to being photometrically classified (type ‘zSNIa’ in Sako et al. 2018).

References: (1) Gilliland et al. (1999); (2) Riess et al. (2001); (3) Suzuki et al. (2012); (4) Riess et al. (2018); (5) Chen et al. (2020); (6) Riess et al. (1999); (7) Hamuy et al. (1996); (8) Riess et al. (2004); (9) Riess et al. (2007); (10) Jha et al. (2006); (11) Jha et al. (2007) and references therein; (12) Milne et al. (2010); (13) Stritzinger et al. (2010); (14) Tsvetkov & Elenin (2010); (15) Zhang et al. (2010); (16) Hsiao et al. (2015); (17) Krisciunas et al. (2017a); (18) Burns et al. (2018); (19) Contreras et al. (2010); (20) Gall et al. (2018); (21) Wee et al. (2018); (22) Burns et al. (2020); (23) Kawabata et al. (2020); (24) Stahl et al. (2019); (25) Hicken et al. (2012); (26) Brown et al. (2014); (27) <https://pbrown801.github.io/SOUASA/>; (28) Krisciunas et al. (2017b); (29) Ganeshalingam et al. (2010); (30) Hicken et al. (2009); (31) Guy et al. (2010); (32) Foley et al. (2018); (33) Scolnic et al. (2021); (34) Brout et al. (2019); (35) Smith et al. (2020a); (36) Scolnic et al. (2018); (37) Sako et al. (2018).

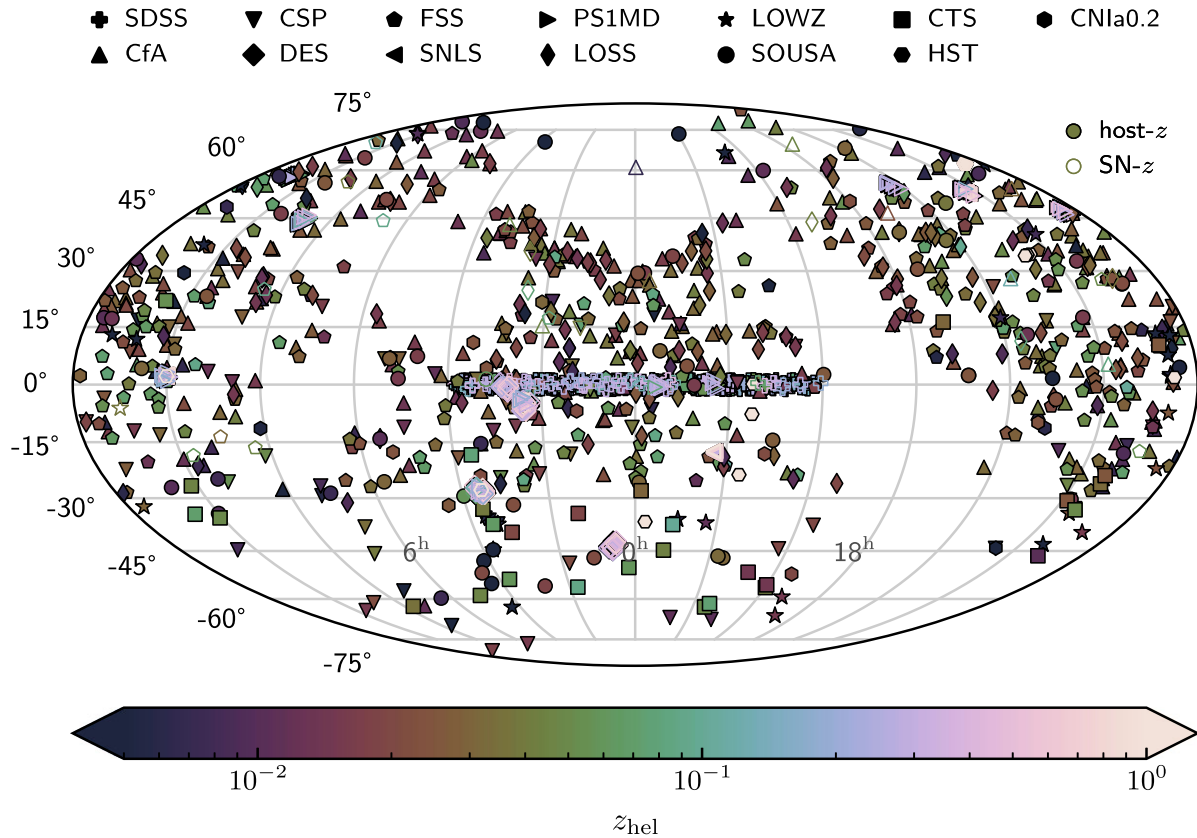


Figure 1. Distribution of Pantheon+ SNe across the sky. Many SNe are common between samples, but only one sample is picked to represent each SN. Redshifts from the host galaxies are represented by black-outlined solid symbols, and redshifts from supernova spectra are colour-outlined unfilled symbols. Several samples (generally at higher z i.e. SNLS, DES, PS1MD, HST) targeted small sky areas repeatedly, so many SNe are confined to small patches. These patches are visible where many lighter, unfilled symbols overlap (these groups obscure the underlying host galaxy redshifts which are always the majority).

2.2 Corrections and additions to previous data

Pantheon+ carries over the same SNe from Pantheon and includes many more SNe from FSS, DES, LOSS, SOUSA and CNIa0.02, as defined in Scolnic et al. (2021). Therefore, redshift and bookkeeping mistakes are carried over from Pantheon which were in turn carried over from their original sources, mostly from older SN compilations. After examining each of the samples listed in Table 1 we found and fixed various errors, and added improvements as follows:

- GOODS+PANS and SCP had Right Ascension (RA) and Declination (Dec) listed as zeros. As a result, the heliocentric corrections had been made to the incorrect part of the sky. We assign coordinates from the original datasets (Riess et al. 2004; Riess et al. 2007; Suzuki et al. 2012) and recompute z_{CMB} .
- We provide updates to DES redshifts from their 3-yr values (Smith et al. 2020a) to their (previously unpublished) values that will be used in DES 5-yr cosmology. This includes reassigning uncertainty based on whether the redshift comes from the host or SN spectrum: 5×10^{-4} and 5×10^{-3} respectively.
- All SCP and GOODS+PANS SNe had redshift uncertainties set to 1×10^{-3} regardless of redshift source, so we reassigned the uncertainties the same way as with DES.
- Six FSS SNe had coordinates that disagreed with both the NED entry and FSS-assigned-host by up to tens of degrees. We

therefore correct the SN coordinates to the NED coordinates, as listed in Table 3.

- One Cfa4 SN had its location mistaken for a SN discovered around the same time. The record for 2008cm had the coordinates of SNF 20080514-002, but since the redshift was in agreement with the host of 2008cm, we update the SN coordinates using NED (Table 3).
- We update the coordinates of Cfa1 SN 1996C to those of SIMBAD because the NED coordinates are incorrect (Table 3).
- Where we have identified the host of a SN, host coordinates are provided separately to SN coordinates. There was previously no record of SN hosts in Pantheon or some source catalogues. Heliocentric corrections are performed using host coordinates where possible.
- Where an International Astronomical Union name (IAUC) for a SN exists, we record it alongside the internal ID (SNID). The IAUC links SNe that are common across samples that use different internal names. However, we recommend that in future, a dictionary of all names for a SN be implemented since SNe without an IAUC must be matched via position instead.
- In collaboration with Peterson et al. (2021), we include group-centre coordinates and group-average heliocentric redshifts, from which we derive group z_{CMB} , group z_{HD} and group v_p (see Table 2).

Table 2. Master table of updated redshifts. Symbols are defined in Section 2.1. The full machine readable table is available online from VizieR and at <https://github.com/PantheonPlusSH0ES/DataRelease>. The online versions of this table include columns for peculiar velocity uncertainty and binary classifications for if a SN has an associated host, if the redshift is from a host and if the supernova has group values. All peculiar velocities have an uncertainty of 250 km s^{-1} , and all z_{hel} share the same uncertainty as their corresponding z_{CMB} . Blank entries for group information mean the SN has no associated group, and blank IAUC entries mean there is no IAU name for the SN.

SNID	IAUC	Host	SN RA ° (J2000)	SN Dec ° (J2000)	Host RA ° (J2000)	Host Dec ° (J2000)	z_{hel}	z_{CMB}	$\sigma_{z_{\text{hel}}}$	z_{HD}	$\sigma_{z_{\text{HD}}}$	v_p km s ⁻¹	Group RA ° (J2000)	Group Dec ° (J2000)	Group z_{hel}	Group z_{CMB}	Group z_{HD}	Group v_p km s ⁻¹
2001G	2001G	MCG +08-17-043	137.38825	50.28092	137.38721	50.28186	0.016703	0.017272	1.1×10^{-5}	0.01770	8.5×10^{-4}	-127
2001V	2001V	NGC 3987	179.35388	25.20250	179.33717	25.19539	0.015007	0.016045	9.0×10^{-4}	0.01570	1.2×10^{-3}	102	179.514560	25.171888	0.014883	0.015920	0.01557	102
2001ah	2001ah	UGC 06211	167.62425	55.16083	167.62646	55.16983	0.057763	0.058373	1.5×10^{-5}	0.05886	8.8×10^{-4}	-138
2001az	2001az	UGC 10483	248.61546	76.02967	248.62017	76.02972	0.040695	0.040593	9.0×10^{-5}	0.04101	8.7×10^{-4}	-121
2001da	2001da	NGC 7780	358.38658	8.11739	358.38404	8.11814	0.017381	0.016148	7×10^{-6}	0.01659	8.5×10^{-4}	-129	358.404510	7.930666	0.017816	0.016583	0.01702	-176
2001en	2001en	NGC 0523	21.34542	34.02514	21.33637	34.02494	0.015881	0.014937	7×10^{-6}	0.01509	8.5×10^{-4}	-46	21.041921	33.581505	0.016294	0.015343	0.01550	-46
2001fe	2001fe	UGC 05129	144.48792	25.49481	144.49167	25.49478	0.013514	0.014478	8×10^{-6}	0.01467	8.5×10^{-4}	-57
2001gb	2001gb	IC 0582	149.75400	17.82011	149.75096	17.81714	0.025439	0.026529	1.1×10^{-5}	0.02650	8.6×10^{-4}	9
2001ic	2001ic	NGC 7503	347.68058	7.56956	347.67617	7.56769	0.044089	0.042802	9×10^{-6}	0.04390	8.7×10^{-4}	-317
2002bf	2002bf	CGCG 266-031	153.92629	55.66853	153.92604	55.66747	0.024376	0.024936	7×10^{-6}	0.02525	8.6×10^{-4}	-92

Table 3. Corrections to SN positions.

SNID	Prev. RA ° (J2000)	Prev. Dec ° (J2000)	Updated RA ° (J2000)	Updated Dec ° (J2000)
1996C	207.75158	+49.341251	207.7025	+49.31864
2008cm	202.30344	+11.272403	109.16146	−62.31469
vespasian	215.136083	+53.046728	322.4275	−7.69658
ASASSN-15ga	208.159615	+10.718024	194.86372	+14.17105
SN2016aqb	164.193214	−13.047481	170.49333	−13.98367
ATLAS16bww	93.620268	−17.421361	18.59275	−13.15309
PS16bnz	158.658125	+27.190117	155.15375	−2.46675
PS16eqv	53.168411	−19.615435	37.93083	−25.00162
ASASSN-17aj	101.946198	+7.920005	173.29375	−10.22177

As a result of these changes, all SNe now have the same information: both the SNID and IAUC where applicable, both SN and host co-ordinates where applicable, redshifts in the heliocentric and CMB frame, and finally our updated peculiar velocities.

3. Reviewing heliocentric redshifts

The most accurate redshift for a SN—in the absence of a galaxy group average redshift—is that of its host galaxy, so it is imperative that the correct host is assigned. This is true at any redshift, but especially so at low redshift. In this work, we define the low- z sample as the ~ 1000 galaxies with $z \lesssim 0.12$ (median $z \sim 0.024$). These are primarily the SNe that were not uniquely observed in the typical ‘high- z ’ surveys of SNLS, DES, SDSS, PS1MD and HST, however some SNe in these surveys are low- z since they were also observed by the low- z surveys.

In the interest of thoroughly reassessing the redshifts of Pantheon+, we used Aladin (Bonnarel *et al.* 2000) to visually inspect Pan-STARRS images at every low- z (and occasionally moderate- z) SN location, to assign and record hosts. It is this requirement of visual inspection that makes our definition of low- z unique. We also used Dark Energy Camera Legacy Survey, SDSS and DES images where available, and for Dec $\lesssim -30^\circ$ we used mostly Digitized Sky Survey 2 images. For the hosts we identified, we chose the ‘best’ redshift according to a hierarchy of criteria outlined below. For the three low- z SNe we could not assign hosts—1996ab, 2007kg and 2008dx—we use the redshift given in the original classification reports. Apart from these three, there was ambiguity in only six low- z hosts (see discussion below). In addition the low- z sample for which we identified redshifts, we confirmed the coordinates and host names of all SDSS and FSS SNe.

Some redshifts in NED are supplied with a comment as to their origins, which contribute to picking the best redshift. The origins are either ‘from new data’ (i.e. the reference measured the redshift), ‘from reprocessed raw data’, or ‘from uncertain origins’. Most redshifts are from uncertain origins, usually because the sources re-record older redshifts, but also because some NED records do not report that the redshift is new.

The criteria for picking the best redshift are:

1. We use SDSS Data Release 13 (DR13) redshifts when they are available, as these are usually the most up-to-date measurement, have low uncertainty, and show stability in that earlier iterations of SDSS tend to converge on the DR13 values.

2. Next we consider other sources that include uncertainty estimates. Among these we choose the one that first satisfies, in order of decreasing priority:

- (a) The most recent source that has taken new data and measured a new redshift.
- (b) The most recent source that has reprocessed old data.
- (c) The most recent source that has an uncertain origin. This may be original data, but may also be from a new publication that uses old redshifts because these often appear as new entries in NED. We endeavoured to avoid republished redshifts and quote the original source.

In the case of multiple redshifts satisfying any condition, we take the most precise redshift.

3. If none of the above criteria are satisfied we consider redshifts that lack an uncertainty estimate, but are not a SN redshift. In these cases, we set the uncertainty to 9×10^{-5} (see Section 4).
4. As the last resort we take the redshift derived from the original SN spectrum. In the cases where no redshift uncertainty is reported, we set the uncertainty to be 5×10^{-3} (Section 4).

We examined all redshifts in the low- z sample except those that come from FSS. These redshifts were *not* updated because FSS adopt their own hierarchical approach to selecting redshifts in the literature (Foley *et al.* 2018). Importantly, FSS measure new host redshifts for SNe previously without host redshifts. Thus, we assume this sample has the best existing redshift estimates already.

Out of 2285 unique SNe Ia, 990 heliocentric redshifts have been updated. This is mainly for low- z hosts, whose redshifts have been measured multiple times. Some notable cases:

- All HST supernovae had z_{hel} listed as z_{CMB} . In each case, we use the heliocentric redshifts given by the original publication and recompute z_{CMB} .
- SN 1992bk, 2000cp, 2008bf, 2008ff, 2009eu, 2014at and PSNJ1628383 each occurred in a group of galaxies so that a unique host could not be determined. The most accurate treatment of these cases, and in fact in general, is to average the redshifts of host-galaxy-group members, as in Peterson *et al.* (2021), with more members giving a more accurate redshift. Figure 2 shows images for these six cases, with SN locations and potential hosts indicated. We set the group redshift uncertainty to the dispersion in group member redshifts. SN 1992bk is a good example of how the ‘directional light radius’ (DLR; see Gupta *et al.* 2016) might be used to exclude the smaller, less likely cluster galaxies from being considered as hosts. We do not use DLRs to determine the most likely host, and instead visually identify the most likely group members and take their average redshift, which gives a more accurate estimate of the Hubble-flow redshift than any single group member.
- Some SNe had multiple unique SDSS redshift measurements from the same data release. The unique redshifts were averaged, and uncertainties estimated from the dispersion of redshift measurements, similar to the ambiguous host redshifts (see Table A1). The quoted redshift uncertainties are often less than the standard deviation of the measurements (despite the fact that standard deviations measured from small samples are typically underestimated) indicating that the redshift uncertainties may be underestimated; see discussion in Section 4.

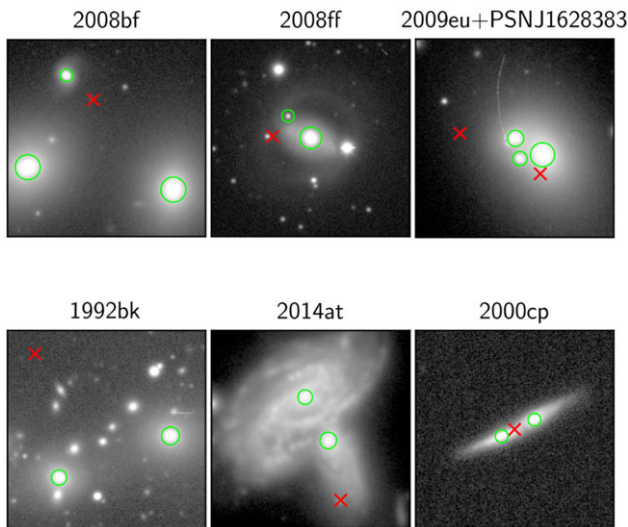


Figure 2. All instances of an ambiguous host where redshifts of multiple likely hosts have been averaged (in each case all possible hosts are at approximately the same redshift). In all images, North is up and East to the left. Red crosses indicate the location of the SN, and green circles indicate the hosts used. Other objects in the images were not selected because they were stars, or were less likely host galaxies due to their size.

- There were many cases where a SN redshift was quoted in place of a more accurate host redshift, as seen in the discrepancies between the four different redshift sources Sako et al. (2018, Tables 1 and 9), Gupta et al. (2011), and Östman et al. (2011). We examined every image of SDSS SNe to confirm the host, SN coordinates, and attempt to update the redshift using NED. In ambiguous host cases, we use the host coordinates published in Sako et al. (2018). In this way, we replace 81 SN redshifts with host redshifts.
- Zheng et al. (2008) noted in the first year SDSS SN data release that there was a systematic offset of 3×10^{-3} between host redshifts and SN redshifts, and thus they applied the shift to SN redshifts to bring them in line with host redshifts. Sako et al. (2018) found a similar offset of $(2.2 \pm 0.4) \times 10^{-3}$ was present in their larger sample of SDSS SNe, however they did not apply the shift to the SN redshifts. We confirm that we see the same trend in the 81 SDSS SNe whose SN- z we replace with host- z . Unlike Sako et al. (2018), we *do* apply this systematic redshift shift of $+2.2 \times 10^{-3}$ to the remaining 46 SDSS SN- z s.^c

Table A2 shows the largest disagreements between new and old redshifts in decreasing level of disagreement, with justifications for the update. Since we expect updates from SN- z to host- z to be large, we focus on disagreements between host- z s.

4. Estimating redshift uncertainties

Ideally, each object would have an individual redshift uncertainty measurement based on its spectrum. However, many surveys (generally those at higher redshift) do not provide this information and instead give overall estimates of redshift uncertainties for typical classes of object (e.g. DES, PS1MD, SNLS; see Figure 3). There are several ways to estimate the redshift of an object: emission-line

^cRedshifts are added together by multiplying $1+z$ factors, however here we apply the correction additively, which we believe is how the systematic offset was modelled.

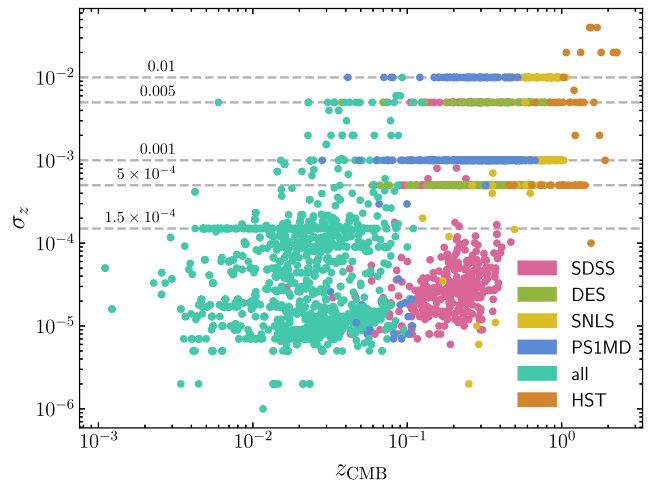


Figure 3. Uncertainty in redshift versus redshift. We observe a general upward trend with redshift as expected. Samples that use standard uncertainties have been highlighted with dashed lines. The standard uncertainty of 1.5×10^{-4} is that of the 6dF redshifts in the low- z sample.

redshifting (e.g. Colless et al. 2001), cross-correlation with templates (Tonry & Davis 1979), least-squares minimisation (Bolton et al. 2012), or from 21 cm H I emission profiles in radio (e.g. Springob et al. 2005). Each method has its own way of estimating redshift uncertainty per spectrum, and the Pantheon+ sample has redshifts determined from each of these methods. For instance, SDSS uses least-squares minimisation, DES/OzDES uses cross-correlation, there are many galaxies with 21 cm H I redshifts (mostly from Springob et al. 2005), and many more that are unspecified.

4.1 Typical uncertainties

More problematic than reporting only class-based uncertainties is the non-reporting of uncertainties. Some SN data releases did not include uncertainties (e.g. CSP, CfA), in which case the only way to obtain an uncertainty estimate is to instead use an original measurement of the redshift. Our aim is for every redshift to have an uncertainty estimate, so we must estimate uncertainties where none are reported. Despite identifying the best primary source according to the hierarchy above, a small number of sources did not provide uncertainties. With no information about the spectra themselves, we opt to set missing uncertainties to a typical value, according to whether they are host or SN redshifts.

We examine the redshift uncertainties of five surveys with redshifts in Pantheon+ or that provide their own galaxy redshift uncertainty statistics: the Two-degree Field Galaxy Redshift Survey (2dFGRS; Colless et al. 2001), the WiggleZ Dark Energy Survey (Drinkwater et al. 2018), SDSS, DES/OzDES (Lidman et al. 2020) and the Digital Archive of H I 21 Centimeter Line Spectra from Springob et al. (2005). However, we defer the discussion of SDSS-measured redshifts to Section 4.2 as SDSS redshift uncertainties are consistently smaller than other optical estimates.

While each method of redshifting naturally provides a way of estimating uncertainty, the more common way to estimate uncertainty is by comparing multiple measurements of the same object. Each survey found:

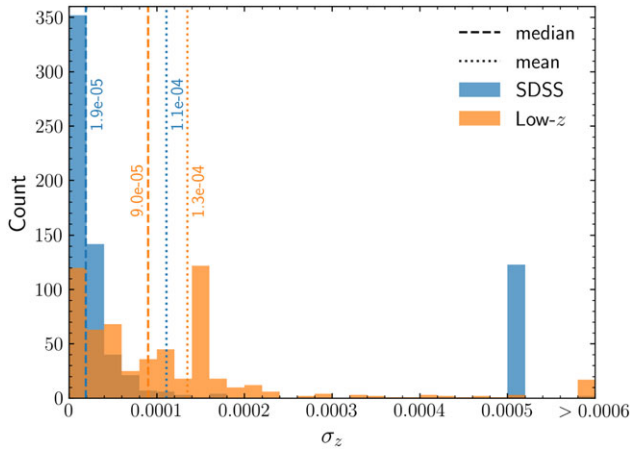


Figure 4. Comparison of SDSS DR13 redshift uncertainties and all other low- z SN uncertainties. SDSS DR13 has a tight distribution peaking around 1×10^{-5} , while low- z is much broader due to its heterogeneous redshift sub-samples. Redshifts larger than 0.0006 have been collected into a single bin, as the maximum is 0.002 (Perlmutter et al. 1999). The spike in low- z at $\sigma_z = 0.00015$ is due to 6dF, while the SDSS spike at $\sigma_z = 0.0005$ corresponds to the uncertainty typically set for a redshift from emission/absorption lines in a SN spectrum.

- 2dFGRS: Over $0 < z < 0.3$, the RMS of multiple measurements was $\sigma_z = 2.8 \times 10^{-4}$. The authors found a slight upwards trend with redshift.
- WiggleZ: Over $0 < z < 1.3$, the standard deviation of multiple measurements ranged from $\sigma_z = 1.7 \times 10^{-4}$ for the highest quality spectra to $\sigma_z = 2.7 \times 10^{-4}$ for the lower quality but successfully redshifted spectra. The authors found no trend with redshift.
- OzDES: The collaboration opted to estimate uncertainties for classes of objects, assigning general SN host galaxies uncertainties of $\sigma_z = 1.5 \times 10^{-4}$, which the authors state is a lower bound.^d
- Springob et al. (2005) 21 cm Archive: Compared with optical, redshifts determined from the 21 cm line offer impressive precision. After reanalysing nearly 9000 nearby ($-0.005 < z < 0.08$) H I galaxies, the mean and median redshift uncertainty was 1.7×10^{-5} and 1.2×10^{-5} respectively.

For the Pantheon+ low- z sample, which has a mix of optical and radio redshifts from the literature, we find a median redshift uncertainty of 9×10^{-5} , which is consistent with the above measurements. We also include in this test the 30 PS1MD and SNLS SNe whose host galaxies we find third party redshifts for, extending to $z \sim 0.50$. We show in Figure 4 the distribution of the redshift uncertainties of this modified low- z sample. Since there remain 30 host galaxies that lack redshift uncertainties, all at low- z , we opt to assign the median uncertainty calculated from the rest of our low- z sample (see Table A3).

Until now, we have discussed only host galaxy redshifts because these have been studied in detail. Estimating redshifts from SN spectra has had less attention. Like host galaxy redshifts, there are SN redshifts without uncertainty estimates. In these cases, we rely on a less concrete estimation of $\sigma_z = 0.005$, based on the population of SN redshifts to date and expert opinion. We reiterate that

^dTo be conservative we have set the host galaxy redshift uncertainty for DES SNe that are in Pantheon+ to be 5×10^{-4} (M. Smith, private communication).

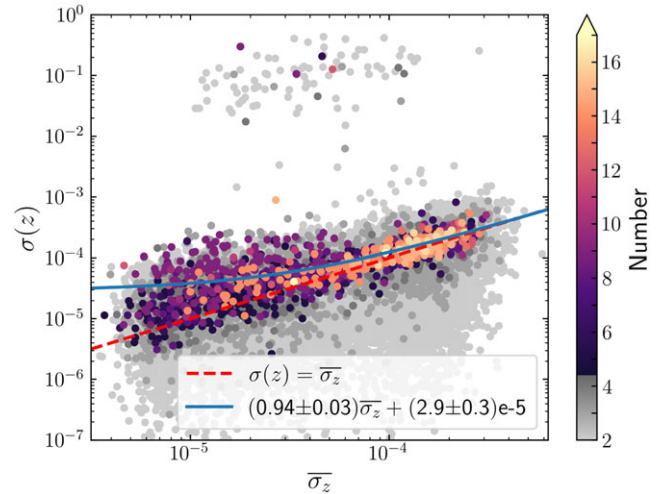


Figure 5. Standard deviation of multiple SDSS DR13 reliable redshift measurements of the same object against the average of their quoted uncertainties. We expect a slope of 1.0 (red dashed line) if the uncertainties are appropriate. The solid blue line is a linear fit to all data with five or more measurements and a dispersion of $\sigma(z) < 0.01$, which shows that, consistently, $\sigma(z) > \bar{\sigma}_z$. Every point with $\sigma(z) \gtrsim 0.01$ is a catastrophic redshift failure caused by at least two distinct confident redshifts.

this is a somewhat conservative but fair estimation. As an example, as given by SNID (Blondin & Tonry 2007), the mean redshift uncertainty of the 51 supernovae with Type Ia SNID classifications from the CfA Supernova Group website^e is $\sigma_z = 4.1 \times 10^{-3}$ with a standard deviation of 1.7×10^{-3} .

See Table A3 for a list of all SNe previously missing uncertainties.

4.2 Underestimated SDSS uncertainties

We noted in Section 3 that when multiple redshift measurements were available in SDSS, the dispersion in redshift values is usually higher than expected from their typical uncertainties of 1×10^{-5} . This comparison indicates that typical SDSS redshift uncertainties are somewhat optimistic. We quantify this comparison by calculating both average uncertainty, $\bar{\sigma}_z$, and dispersion in z , $\sigma(z)$, for all multiply-measured objects in SDSS DR13. Only objects with two or more reliable redshifts are used.

The average uncertainty versus z dispersion for all multiply-measured objects is shown in Figure 5. We perform a linear fit to the objects with five or more measurements weighted by number of redshift measurements. Calculating standard deviation from few points is systematically biased low (grey points), so we exclude objects with two–four measurements. We also exclude dispersions above 0.01 since these dispersions are caused by multiple confident but disparate redshifts. Thus the fit was performed on 1000 of 31000 objects.

The uncertainty of 9×10^{-5} that we apply to sources with no provided uncertainty reflects the mean dispersion of 9.5×10^{-5} we calculate for repeated non-outlying SDSS measurements. Since we see a gradient of almost unity and a positive offset of roughly 3×10^{-5} between dispersion and estimated uncertainty, increasing the SDSS uncertainties by this amount would be reasonable, and

^e<https://lweb.cfa.harvard.edu/supernova/OldRecentSN.html> and <https://lweb.cfa.harvard.edu/supernova/RecentSN.html>.

we test the impact of this increase in our cosmological analysis in Section 7.^f

5. Combining redshifts multiplicatively

5.1 Heliocentric corrections

Most publicly available heliocentric corrections, including those currently in NED and Pantheon used a low-redshift approximation (although the approximation in NED will be corrected; see Carr & Davis 2021). When performing the heliocentric correction, the low-redshift approximation assumes the observed redshift z_{hel} is an *additive* combination of z_{CMB} and the redshift due to our Sun’s peculiar motion, z_{Sun} ,

$$z_{\text{hel}} = z_{\text{CMB}}^+ + z_{\text{Sun}}. \quad (1)$$

However, the correct way to combine redshifts is to multiplicatively combine factors of $(1 + z)$, so

$$(1 + z_{\text{hel}}) = (1 + z_{\text{CMB}}^x)(1 + z_{\text{Sun}}). \quad (2)$$

This gives the correct CMB-frame redshift, which is

$$z_{\text{CMB}}^x = \frac{1 + z_{\text{hel}}}{1 + z_{\text{Sun}}} - 1. \quad (3)$$

The difference between using the additive approximation and the correct multiplicative equation is exactly $z_{\text{CMB}}z_{\text{Sun}}$. Since z_{Sun} is our own motion with respect to the CMB (our velocity v_{CMB} in the direction of the CMB dipole), it is of order 10^{-3} . Therefore, at low- z , the difference between z_{CMB}^x and z_{CMB}^+ appears almost negligible; however, by $z \sim 1$, the error is on the order of 10^{-3} , which is an order of magnitude larger than most reported statistical uncertainties in redshifts.

We have ensured that all sub-samples in the new Pantheon+ sample consistently use the multiplicative correction.

5.1.1 Which dipole to use?

The Pantheon sample mostly used the CMB dipole measured by the Cosmic Background Explorer (COBE) satellite (Fixsen et al. 1996), in the direction of galactic longitude and latitude $(l, b) = (264.14^\circ \pm 0.30^\circ, 48.26^\circ \pm 0.30^\circ)$ with a velocity $v_{\text{Sun}}^{\text{COBE}} = 371 \pm 1 \text{ km s}^{-1}$.

We update the heliocentric correction to use the dipole measured by the Planck Collaboration (Planck Collaboration et al. 2020), $(l, b) = (264.021^\circ \pm 0.011^\circ, 48.253^\circ \pm 0.005^\circ)$ with a velocity $v_{\text{Sun}}^{\text{Planck}} = 369.82 \pm 0.11 \text{ km s}^{-1}$. The difference in redshift between using the COBE dipole and the Planck dipole is at most $\sim 10^{-5}$, so this is a small change.

5.1.2 Calculating z_{Sun}

The projection of the Sun’s peculiar velocity along the line of sight to an object is

$$v_{\text{Sun}} = \mathbf{v}_{\text{Sun}} \cdot \hat{\mathbf{n}}_{\text{obj}} = v_{\text{Sun}}^{\text{max}} \cos \alpha, \quad (4)$$

where $\hat{\mathbf{n}}_{\text{obj}}$ is the object’s position vector, and α is the angle separating the dipole direction and the object.

^fOur increased uncertainty better reflects the observed dispersion between SDSS measurements but may still underestimate the uncertainties given the typical uncertainty of optical redshifts in Section 4.1.

Since the Sun’s velocity is small (order of 10^2 km s^{-1}) compared to c , the low- z approximation $z_{\text{Sun}} \approx -v_{\text{Sun}}/c$ is adequate, but we use the full special relativistic calculation

$$z_{\text{Sun}} = \sqrt{\frac{1 + (-v_{\text{Sun}})/c}{1 - (-v_{\text{Sun}})/c}} - 1, \quad (5)$$

because there is negligible computational advantage to the approximation. The minus signs before v_{Sun} have been left explicit to emphasise that at zero angular separation ($\alpha = 0$ in Equation (4)) the object should appear slightly blueshifted due to our velocity directly towards it.

5.2 Peculiar velocity corrections

The peculiar redshifts arising due to the peculiar velocities of the supernova host galaxies also need to be treated multiplicatively. Equation (2) becomes

$$(1 + z_{\text{hel}}) = (1 + z_{\text{HD}})(1 + z_{\text{Sun}})(1 + z_{\text{p}}). \quad (6)$$

Here we use the ‘Hubble diagram redshift’ z_{HD} , which is the cosmological redshift we are interested in. This differs in our nomenclature from the CMB-frame redshift z_{CMB} , because z_{CMB} takes into account our motion but *not* the peculiar velocity of the source. Combined with Equation (2) we see

$$z_{\text{HD}} = \frac{1 + z_{\text{CMB}}}{1 + z_{\text{p}}} - 1. \quad (7)$$

Thus the Hubble diagram redshift requires knowledge of the SN host’s peculiar redshift z_{p} , so we turn to how we derive peculiar velocities.

6. Updating peculiar velocity modelling

By applying the heliocentric-to-CMB correction we have accounted for the motion of our own solar system with respect to the CMB. However, we have not yet accounted for the peculiar velocity of the supernova’s host galaxy (v_{p}). Removing the redshift due to the estimated peculiar velocity of the host galaxy leaves the cosmological redshift z_{HD} (Equation (7)), which is the redshift needed for the Hubble diagram.

In this section, we describe the methodology for computing the peculiar velocity for each host galaxy. Our treatment differs from the peculiar velocities used in Pantheon in the following ways:

- We use the multiplicative equation for combining redshifts (Equation (6)).
- We convert the predicted peculiar velocity field to redshift-space (Section 6.2).
- Outside the measured peculiar velocity field we model the residual bulk flow as a decaying function, rather than a constant external velocity (Section 6.3).
- We flip the v_{p} sign convention used in the Pantheon sample (and effected the same change in the SuperNova ANALYSIS software (SNANA, Kessler et al. 2009) as of version 11.02). Now, v_{p} is positive when moving away from us, which is consistent with the sign of recession velocities.

The nominal set of peculiar velocities we derive here are examined in the companion paper Peterson et al. (2021) in the context of the efficacy of different peculiar velocity samples, models and parameters of our own model on SN Hubble residuals.

6.1 Estimating peculiar velocities

The most precise way to estimate peculiar velocities is to measure the density field (e.g. through a redshift survey) and use that to predict the expected peculiar velocity field.⁸ This is known as *velocity field reconstruction*. Importantly, this method does not use supernova distances, and therefore does not introduce correlations between the peculiar-velocity-corrected SN redshift and its measured distance. The reconstruction does require an assumed cosmological model, but the cosmological dependence is weak. We quantify the impact of these peculiar velocity corrections on cosmological parameters in Section 7.

In the linear regime, peculiar velocity is related to the gravitational acceleration via:

$$v(\mathbf{r}) = \frac{f}{4\pi} \int d^3\mathbf{r}' \delta(\mathbf{r}') \frac{\mathbf{r}' - \mathbf{r}}{|\mathbf{r}' - \mathbf{r}|^3}, \quad (8)$$

where f is the growth rate of the cosmic structure and $\delta(\mathbf{r})$ is the density contrast. This equation has two limitations:

- Galaxy surveys do not measure the total matter density, so it is assumed that the observed galaxy density (δ_g) linearly traces the total density, $\delta = \delta_g/b$. Here b is the linear biasing parameter, which is different for different types of galaxies, and therefore has to be measured or marginalised over.
- The region over which we have a sufficient number density of measured galaxies to do reconstruction is smaller than the region for which we need to estimate peculiar velocities. This has been addressed by estimating the ‘external velocity’, \mathbf{V}_{ext} , which arises due to structures outside the survey volume, and estimating how that would theoretically decay with distance (Section 6.3).

We use the velocity field reconstruction created by Carrick et al. (2015), which uses data from the 2M++ compilation from Lavaux & Hudson (2011). 2M++ includes data from 2MRS (Huchra et al. 2005), 6dFGS (Jones et al. 2009), and SDSS (Abazajian et al. 2009) and extends to a radius of $r_{\text{max}} = 200 h^{-1} \text{Mpc}$. One slice ($SGZ = 0$) of the reconstructed density field is shown in Figure 6 in the supergalactic plane ($SGX - SGY$). Figure 7 shows the 2M++ velocity field in redshift-space on a regular spatial grid.

A key model parameter to evaluate is $\beta \equiv f/b$. The rate of growth is often parameterised by $f = \Omega_m^\gamma$, where $\gamma = 0.55$ in the standard cosmological model, ΛCDM . Importantly, however, β is determined empirically rather than computed from the ΛCDM model.

Both β and \mathbf{V}_{ext} are derived from a combination of density field reconstruction and observation. The reconstruction process delivers a normalised peculiar velocity field, $v_{p,\text{recon}}(\mathbf{r})$, which gives the directions and *relative* magnitudes of the peculiar velocities as a function of position. Predictions from this peculiar velocity field are compared with galaxies that have peculiar velocities derived from distance measures such as the Tully-Fisher relation or Fundamental Plane relation. The calibrated peculiar velocity field is

$$v_p(\mathbf{r}) = \beta v_{p,\text{recon}}(\mathbf{r}) + \mathbf{V}_{\text{ext}}(\mathbf{r}). \quad (9)$$

⁸Directly measuring peculiar velocities using an independent distance measurement (such as the Tully-Fisher or Fundamental Plane relation) is less precise ($\sim 20\%$ uncertainties) and observationally challenging. Due to their sparseness, direct peculiar velocity catalogues are difficult to interpolate to get reliable peculiar velocity estimates for galaxies that do not have direct distance measurements.

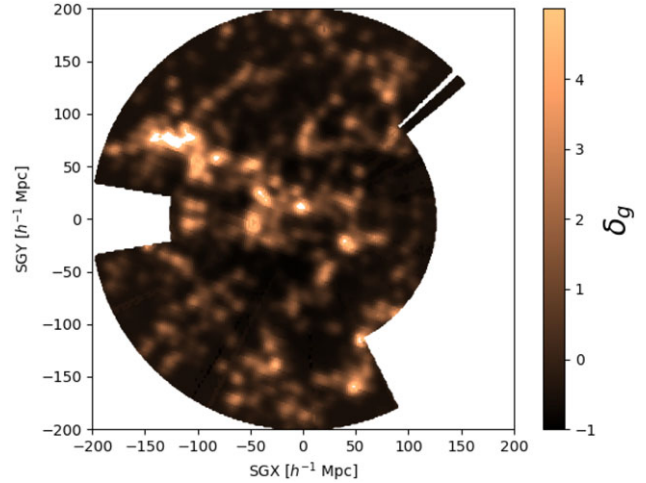


Figure 6. Slice of the 2M++ reconstructed density field plotted in the supergalactic plane ($SGZ = 0$). White areas are regions for which data is missing, therefore the density reconstruction is uncertain.

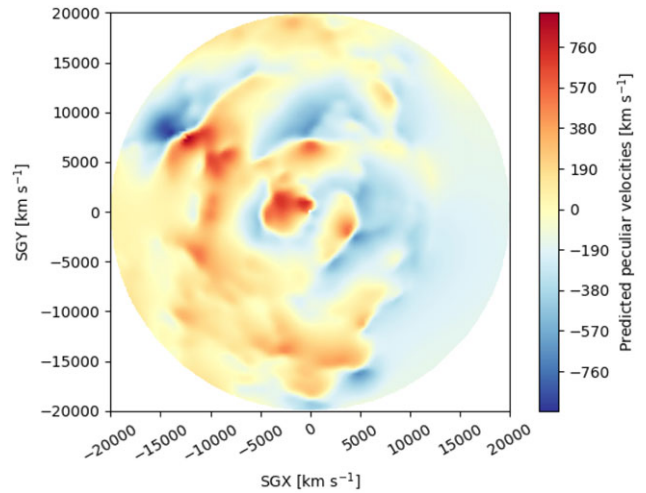


Figure 7. 2M++ velocity field plotted on a regular grid of redshift-space positions. Note the white regions in Figure 6 have been interpolated over to make a complete velocity field out to $200 h^{-1} \text{Mpc}$, which means those regions of the velocity field will have higher uncertainty than other regions.

The parameter β thus acts as a scaling of the normalised velocity field (subject to the sample of observed v_p), and \mathbf{V}_{ext} is the residual mean velocity.

Carrick et al. (2015) measured $\beta = 0.431 \pm 0.021$ and an external velocity of $|\mathbf{V}_{\text{ext}}| = 159 \pm 23 \text{ km s}^{-1}$ in the direction of $(l, b) = (304^\circ \pm 11^\circ, 6^\circ \pm 13^\circ)$. While we use the velocity field measured by Carrick et al. (2015), we use an updated value of $\beta = 0.314^{+0.031}_{-0.047}$ derived in Said et al. (2020), which gives a better fit when comparing SDSS Fundamental Plane peculiar velocities to the predicted peculiar velocity field. We confirm that this lower β value results in a lower scatter in the supernova Hubble diagram, see Peterson et al. (2021).

Carrick et al. (2015) estimated the peculiar velocity uncertainty to be 250 km s^{-1} for the galaxies (the particle velocity field) and 150 km s^{-1} for galaxy groups (the haloes). In other words, the uncertainty on an individual galaxy’s peculiar velocity is higher than the uncertainty on peculiar velocity of the group in which it

resides. We note, however, that some regions of the reconstruction are less certain than others because of incomplete sampling. Unfortunately, sampling is not accounted for in current models, so we adopt the value of $\sigma_{v_p} = 250 \text{ km s}^{-1}$ and leave a more precise estimate of the peculiar velocity uncertainty for future work.

6.2 Real vs redshift-space

Carrick et al. (2015) provide the velocity field in ‘real-space’, so the position and distance of a galaxy can be used to draw the peculiar velocity directly from the modelled velocity field. However, in supernova cosmology, the distance measured via the distance modulus should be independent of the redshift. This distance should *not* be used to predict the peculiar velocity to correct the redshift. Converting the observed redshift to distance (by assuming a cosmology) to estimate the peculiar velocity is valid, but less precise than using the redshift. We therefore convert the reconstructed velocity field of Carrick et al. (2015) to redshift-space. While we assume a cosmology for this conversion, any reasonable choice has a negligible effect on the velocity field. Thus we query the peculiar velocity model using the coordinates of each host galaxy or SN (RA, Dec, z_{CMB}), and Equation (9).

The conversion to redshift-space takes two steps. First, for each real-space grid point i we convert the real-space position, r_i , into redshift position z_i using the predicted peculiar velocity at that grid point, $v_{p,i}$. Second, we use inverse distance weighting to interpolate and adjust the irregularly-spaced grid in redshift-space to a regular grid. This process is described in more detail in Appendix B.

An alternative method is to integrate along the line of sight over real-space. This technique is used by the online tool^h associated with Carrick et al. (2015), which was previously used to estimate the Pantheon peculiar velocities. Both methods agree very well, within the uncertainty, as seen in Figure 8. The mean difference is only 5 km s^{-1} (50 times smaller than the individual uncertainty).

6.3 Velocities beyond r_{max}

It is difficult to properly account for velocities outside r_{max} because we do not have an adequate measurement of the density field to predict individual velocities precisely. However, we expect velocities to continue to behave largely according to the bulk flow trend beyond r_{max} as a consequence of Λ CDM large scale structure. In standard Λ CDM a theoretical bulk flow magnitude of $\sim 20 \text{ km s}^{-1}$ is expected even for a sphere with radius $z \sim 1$ (grey dashed lines in Figure 9). Accordingly, peculiar velocities of galaxies outside r_{max} should not be set to zero.

To ensure a smooth transition across r_{max} we have chosen to model the bulk flow as a decaying function consistent with Λ CDM expectations, and in the direction of the bulk flow of the $200 h^{-1} \text{ Mpc}$ sphere. While there is a Λ CDM model dependence, the impact of this high- z correction on cosmological inferences is small both because the corrections are small (at most $\sim 5 \times 10^{-4}$ when in the direction of the bulk flow), and because at high- z these peculiar redshifts represent a small fraction of the total redshift.

We note that there is a slight difference between V_{ext} and the bulk flow of the $200 h^{-1} \text{ Mpc}$ sphere. The bulk flow of the sphere is the average of the internal velocities (which is small but non-zero), plus the external velocity. We calculate the bulk flow at the $2M++$ maximum radius of $200 h^{-1} \text{ Mpc}$ to be $182 \pm 23 \text{ km s}^{-1}$ in

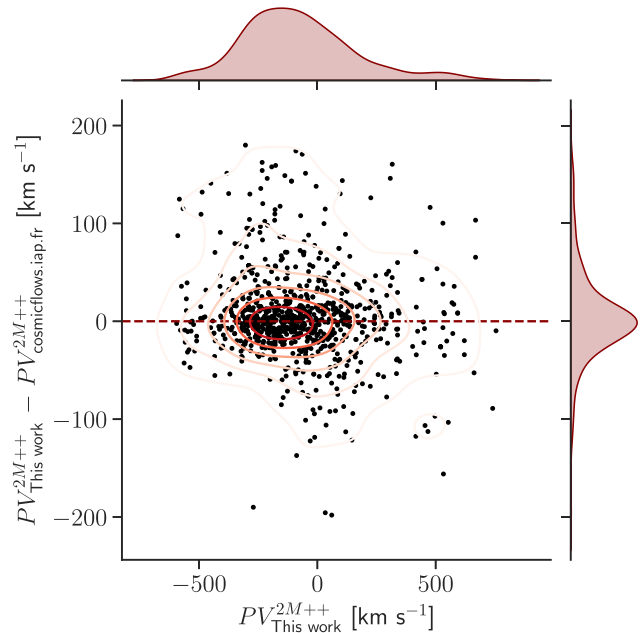


Figure 8. The predicted peculiar velocity for a sample of 851 host galaxies using two different approaches. Each v_p has an uncertainty of 250 km s^{-1} . We use the $2M++$ velocity field converted from real-space to redshift-space whereas the method associated with Carrick et al. (2015) (previously used for Pantheon), integrates over real-space along the line of sight for each host galaxy. There are only negligible systematic differences between the results of these techniques, and all scatter is within 1σ .

the direction of $(l, b) = (302^\circ \pm 10^\circ, 2^\circ \pm 9^\circ)$. At this large radius, the bulk flow is dominated by the external bulk flow ($V_{\text{ext}} \approx 170 \text{ km s}^{-1}$; Said et al. 2020; Boruah, Hudson & Lavaux 2020) plus a small contribution from the mean internal velocities.

Contrary to common expectations, the bulk flow should *not* necessarily converge on the direction of the CMB dipole. The observed CMB dipole is particular to our own motion, and is removed with the correction from the heliocentric to the CMB frame. Dramatic changes to the magnitude and direction of bulk flow direction become unlikely as we average over spheres that approach the scale of homogeneity. Therefore, we fix the direction of the decaying bulk flow in the direction of the $200 h^{-1} \text{ Mpc}$ sphere’s bulk flow.

The Pantheon sample peculiar velocities outside the velocity reconstruction suffered three main issues which can be seen in Figure 9. The most apparent issue is the increasing v_p with redshift. We show that this artefact is caused by the low- z approximation of the heliocentric correction by plotting the error term (i.e. the difference between Equations (1) and (2)) for the four SNLS fields, as these stretch to high- z . This particular error also occurs for PS1MD and SDSS but is less visible since these surveys do not extend as far in redshift. Also visible in Figure 9 are the HST SNe with $v_p = 0$, and the somewhat random scatter around $z \approx 0.15$ which may have been due to assigning $2M++$ peculiar velocities outside the $2M++$ sphere. We show in the bottom panel of Figure 9 that these issues are now resolved.

7. Impact on cosmological parameters

To test the impact of these redshift updates on cosmological parameters we fit for H_0 , and (separately) the dark energy equation of state w , in a flat- w CDM model for various different combinations of updates as listed in Table 4 and described below.

^h<https://cosmicflows.iap.fr>.

Table 4. Impact of different corrections, redshift samples, systematics, and uncertainties on cosmological parameters. We define the change in cosmological parameters to be the variation minus the nominal value (variation 5). N_{SN} refers to the number of supernovae in each sample, which differ between variations depending on which supernovae pass or fail quality cuts as their redshifts change. The uncertainties (σ_{H_0} and σ_w) show only the uncertainty due to the supernova sample size and distance moduli uncertainties, not the expected precision of the measurement.

Variation	Variation description	Total	N_{SN}		ΔH_0	σ_{H_0}	Δw	σ_w
			$0.0233 < z_{\text{HD}} < 0.15$	$z_{\text{HD}} > 0.01$				
0	None	1764	504	1653	-0.12	0.20	0.003	0.045
1	New z_{hel}	1764	500	1653	-0.03	0.20	0.009	0.046
2	New $z_{\text{hel}}, z_{\text{CMB}}^{\times}$	1763	500	1652	-0.02	0.20	0.004	0.046
3	z_{CMB}^{\times} , new v_p	1763	512	1653	-0.06	0.19	-0.008	0.045
4	New z_{hel} , new v_p	1764	512	1654	-0.00	0.19	0.005	0.043
5	Final (all corrections)	1763	512	1653	0	0.19	0	0.044
6	Final, only host-z	1576	495	1466	0.05	0.20	-0.022	0.048
7	Final, group-z, v_p	1764	514	1650	0.05	0.18	-0.011	0.042
8	Final, all $z - \sigma_z$	1764	507	1650	-0.18	0.19	0.011	0.045
9	Final, all $z + \sigma_z$	1766	513	1660	0.20	0.19	-0.015	0.045
10	Final, all $z - 4 \times 10^{-5}$	1765	512	1655	-0.05	0.19	0.013	0.044
11	Final, all $z + 4 \times 10^{-5}$	1762	513	1652	0.06	0.19	-0.012	0.044
12	Final, all $\sigma_z \times 3$	1708	512	1598	0.06	0.19	-0.014	0.045
13	Final, SDSS $\sigma_z + 3 \times 10^{-5}$	1763	512	1653	0.00	0.19	0.000	0.044

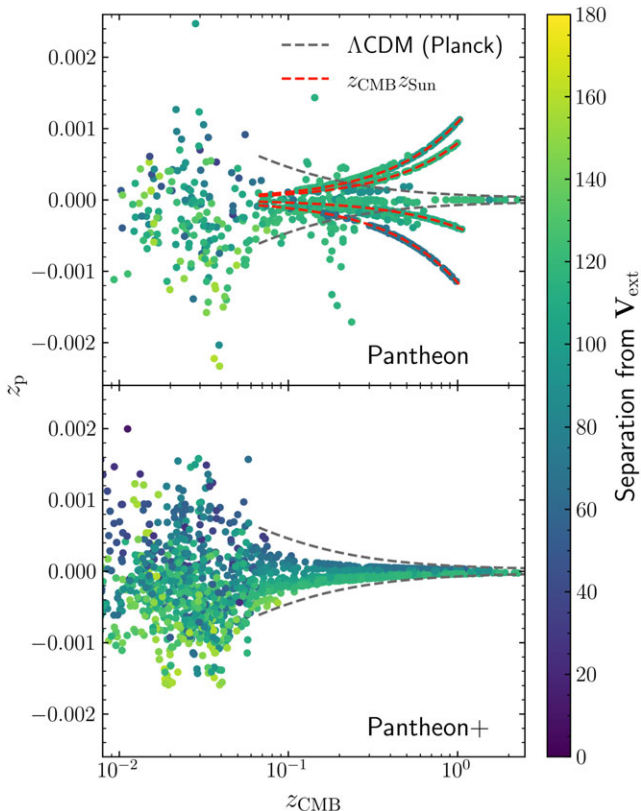


Figure 9. Top: Pantheon (original) peculiar velocities converted to redshift. The expected decay of peculiar velocity amplitude according to Λ CDM is over-plotted (grey dashed), outside the limit of the reconstruction at $200 h^{-1} \text{Mpc}$ ($z \approx 0.067$). The spurious increase in peculiar velocities as redshift increases is driven by the erroneous use of the low-redshift approximation (Equation (1)). The error term is plotted (red dashed) only for the four SNLS fields. Bottom: Pantheon+ (this work) peculiar velocities, converted to redshift, which are now well-behaved beyond low-redshift.

We only report the *changes* in these parameters, relative to the nominal ‘Final’ set that includes all of the updates (updated z_{hel} , exact formula for combining redshifts, and new peculiar velocities). The full Pantheon+ cosmology analysis is reported in Brout et al. (2022).

In addition to combinations of redshift updates, we consider other redshift/sample variations for a total of 14 variations. Each variation is numbered, as listed in Table 4, and the same numbering is also included in each figure for easy reference. The variations we consider are:

- (0) **No corrections** This is the original data without any redshift corrections.
- (1–4) **Partial corrections** These variations are the permutations of (a) updating z_{hel} ; (b) combining redshifts multiplicatively, z_{CMB}^{\times} (as opposed to using the low- z additive approximation); (c) using our new peculiar velocities, v_p .
- (5) **All corrections** The nominal Final data includes all redshift updates.
- (6–7) **Redshift source** We consider first the subset of supernovae that have host-galaxy redshifts (1576 of the 1763 redshifts). Second, for the entire sample we replace host-galaxy redshifts with the redshift of the host galaxy’s group when available (186 of 1763 redshifts).
- (8–11) **Systematic offsets** We consider two different forms of systematic redshift offsets: shifting the redshift by $\pm\sigma_z$ (variations 8, 9), and by $\pm 4 \times 10^{-5}$ (as suggested by Calcino & Davis 2017; Brout et al. 2019) (variations 10, 11).
- (12–13) **Uncertainty changes** The last test is how the size of redshift uncertainties affects cosmological parameters (as suggested by Steinhardt et al. 2020), so we scale all uncertainties up by a factor of 3 (variation 12), and only SDSS-measured redshift uncertainties by $+3 \times 10^{-5}$ (variation 13; see Section 4).

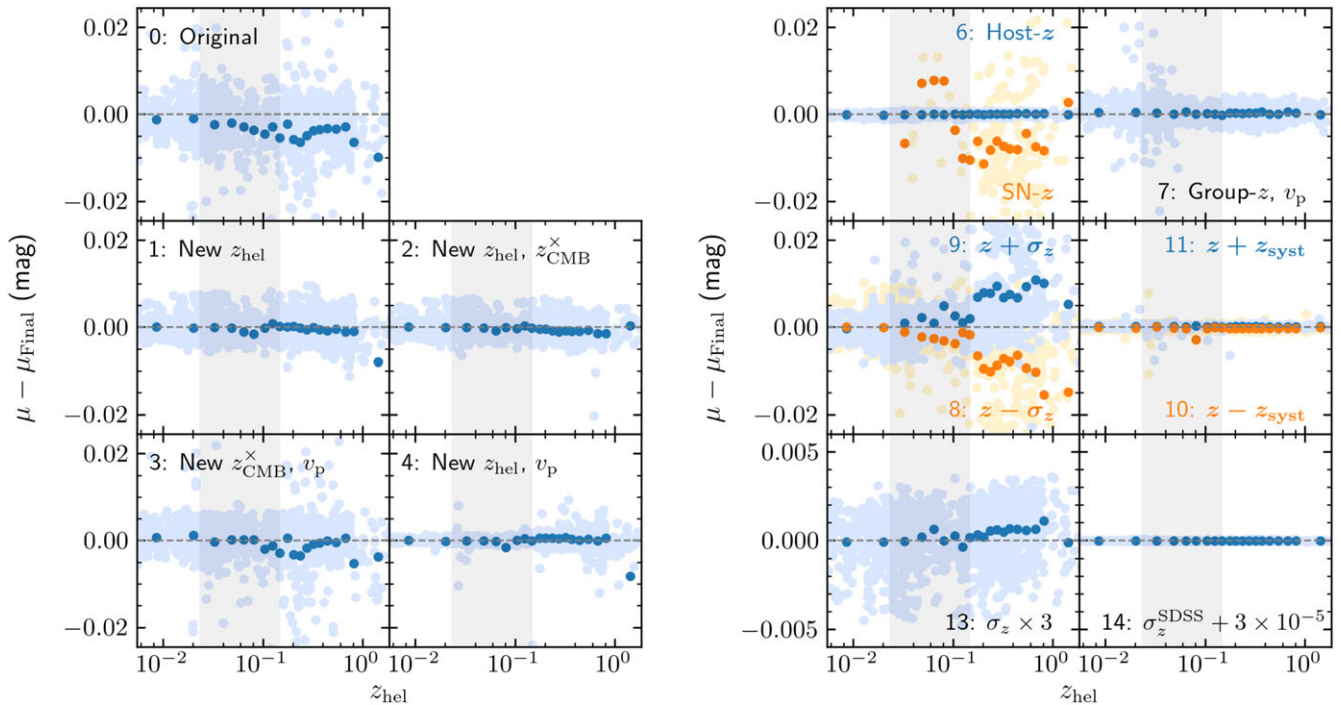


Figure 10. Difference in distance moduli for selected variations compared to the Final values (variation 5), μ_{Final} . Faint points are individual SNe, while dark points are binned in redshift. The grey shaded region represents the redshift range used to fit H_0 . All deviations in the binned differences are within 1σ , where the uncertainty comes only from distance modulus uncertainty (and not absolute magnitude calibration). The largest changes come from the updates to z_{hel} and next largest from the updates to v_p .

In addition, in Section 7.4 we discuss the sub-sample of SNe that lack host- z (187 SNe; the complement to variation 6), but we do not list this as a numbered variation due to the small number of SNe.

7.1 Dependence of distance modulus on redshift change

We analyse each variation independently, meaning that for each: each SN light curve is fit using the SALT2 model Guy et al. (2010) as derived in Brout et al. (2021) using SNANA (Kessler et al. 2009), biases are corrected following the BEAMS with Bias Correction (BBC) framework established in Kessler & Scolnic (2017), and distance moduli μ are determined, all within the PIPPIN framework (Hinton & Brout 2020). The details of this process are given in Brout et al. (2022). The resulting distance moduli changes can be seen in Figure 10.

The total number of supernovae in each variation changes slightly due to various reasons. When we restrict the redshift range for fitting H_0 and w , some borderline-redshift supernovae are shifted in and out of the sample due to redshift changes. However, shifting redshifts also affects the light curve fit parameters. The quality cuts we apply are to these fit parameters (among others) and also their errors. A redshift shift can therefore also shift a supernova in or out of the sample. For example, a light curve parameter may pass the cut with the shifted redshift, or the fit may be poorer at the shifted redshift.

We expect μ to change when a supernova redshift changes because the duration of a light curve (stretch) is affected by time-dilation and its colour is affected by K-corrections, both of which are dependent on the measured heliocentric redshift (but not the peculiar velocity correction); the theoretical basis for these variations is explained in Huterer et al. (2004). However, the distance

modulus of a supernova may also change between sample variations without changing the redshift. The procedure for deriving distance moduli for a supernova sample (e.g. using BBC; Kessler & Scolnic 2017) determines the peak magnitude (m_B) from the light curve, the global parameters α and β that adjust the stretch (x_1) and colour (c) of the supernovae, and a correction term for selection biases ($\delta\mu_{\text{bias}}$), according to a modified version of the Tripp relation (Tripp 1998), following Kessler et al. (2019),¹

$$\mu = m_B - M + \alpha x_1 - \beta c - \delta\mu_{\text{bias}}. \quad (10)$$

Therefore the distance modulus may change even if the redshift is not altered since the calibration of α , β and absolute magnitude (M) depend on the sample as a whole. This explains the slight changes in distance moduli for variation 6 (the host- z sample), in which we do not alter any redshifts.

The dependence of the change in a supernova’s μ between variations on the change in z is demonstrated in Figure 11, which shows that the two are strongly correlated (see also Huterer et al. 2004). This correlation results in a cancellation that reduces the impact of redshift uncertainties, particularly at mid-range redshifts (around $z \sim 0.5$). This can be seen in the solid lines in Figure 11, which show the slope ($d\mu/dz$) of the Hubble diagram at different redshifts. At mid-range redshifts the slope is the same as the degeneracy direction between redshift change and distance modulus change. Thus uncertainties in redshift essentially cancel out at these redshifts, as they cause points to be shifted along the magnitude-redshift relation instead of deviating from it. This

¹In Equation (10) the parameters m_B , $\delta\mu_{\text{bias}}$, x_1 , and c are individual to each supernova, while the parameters M , α , and β are common to the whole population.

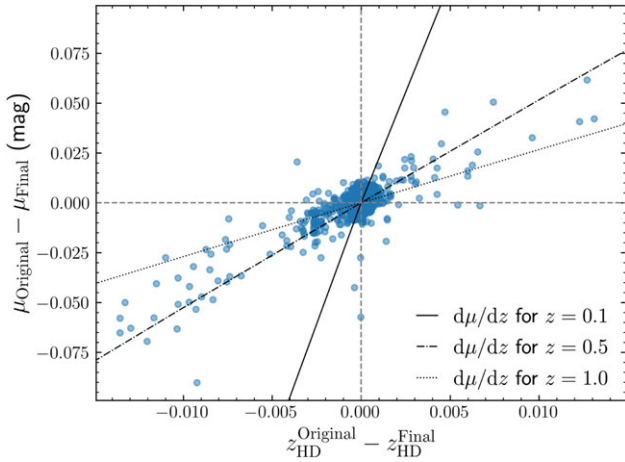


Figure 11. Change in distance modulus versus change in redshift (circles), and $\mu(z)$ derivatives $d\mu/dz$ for given redshifts (black lines). The largest changes occurred due to amending z_{hel} . The black lines represent the purely theoretical $\Delta\mu$ that would occur on the Hubble diagram given the Δz on the horizontal axis (in other words, the slope of the Hubble diagram at those redshifts). The positive trend demonstrates that a change in redshift is partially cancelled the corresponding change in μ (see discussion in Section 7.1). This trend is seen in each variation.

may be particularly helpful for supernova cosmology using photometric redshifts whose uncertainties are larger than spectroscopic redshifts (Chen et al. 2022).

For a simplified assessment of how redshift changes impact cosmology, it is natural to simply use the published μ values, and shift the redshifts (as was done in Davis et al. 2019; Steinhardt et al. 2020). For the low- z sample, we show using the large, transparent symbols in Figure 12 that this gives a reasonable approximation to the full analysis that uses recalculated μ values (smaller symbols). The main difference of not recalculating μ is less cancellation of the effect of systematic redshift changes. At intermediate redshifts one might expect that neglecting the cancellation in $d\mu/dz$ may overestimate the deviation due to redshift shifts. Interestingly, we find that when fitting for w without re-deriving μ the change in w often becomes slightly larger (e.g. variations 0–2) but in some cases (e.g. variations 8–9, shifting the redshifts by $1\sigma_z$) we find the shift in w goes in the opposite direction (likely due to σ_z increasing with z). Overall we find that doing approximate cosmology fits by changing z without changing μ gives reasonable results, but for precision cosmology one should refit μ whenever z_{hel} changes.

7.2 Fitting H_0

We first fit H_0 using the method in Riess et al. (2016), that compares the distance modulus data to a low-redshift approximation of the recession velocity.¹ The only free parameter in this fit is H_0 .

For this fit we focus on only the low-redshift regime of $0.0233 < z_{\text{HD}} < 0.15$, which is the standard range used by previous supernova cosmology analyses such as Riess et al. (2016); Riess et al. (2018). In the Final dataset this redshift range contains 512 SNe of which only 17 lack host galaxy redshifts.

When calculating the uncertainties we only consider the statistical uncertainties in the distance moduli of the supernovae, not the uncertainties in the absolute magnitude calibration. Thus the

¹ $v(z, q_0, j_0) \approx \frac{cz}{1+z} \left[1 + \frac{1}{2}(1-q_0)z - \frac{1}{6}(1-q_0-3q_0^2+j_0)z^2 \right]$, which uses the canonical Λ CDM value of the deceleration parameter $q_0 = -0.55$ and jerk $j_0 = 1$.

uncertainties in H_0 in Figure 12 reflect the size of shifts due only to redshift/sample variations and not the size of uncertainties in the H_0 measurements (for example the current uncertainty on H_0 from SN cosmology is about 5 times larger).

The results are shown in Table 4 and Figure 12, where we see that the redshift improvements we have made have a small impact on the value of H_0 relative to the uncertainty from the SH0ES H_0 measurement with uncertainty of $1.0 \text{ km s}^{-1} \text{ Mpc}^{-1}$ (Riess et al. 2022). We define the difference in cosmological parameters for each variation to be the variation minus the Final value, that is $\Delta H_0 = H_0^n - H_0^{\text{Final}}$ for variation n . Applying all updates to the original redshifts results in $\Delta H_0 = -0.12 \text{ km s}^{-1} \text{ Mpc}^{-1}$. The largest redshift variations, that is shifting all redshifts by their 1σ uncertainties (variations 8 and 9) result in $|\Delta H_0| \leq 0.2 \text{ km s}^{-1} \text{ Mpc}^{-1}$.

7.3 Fitting w CDM

We also evaluate the impact of the redshift updates on the best fit parameters in the flat- w CDM model. This model has two free parameters: the matter density Ω_m , and the equation of state of dark energy w , but we implement a Planck-like prior on the matter density of $\Omega_m = 0.311 \pm 0.010$ so we can isolate the impact on w . We marginalise over absolute magnitude and H_0 , and we fit over the redshift range $z_{\text{HD}} > 0.01$. To estimate the changes in w we use the fast minimisation routine `wFit` in SNANA (Kessler et al. 2009) which outputs marginalised cosmology parameters w and Ω_M ; the complete fit with a thorough covariance analysis can be found in Brout et al. (2022).

The results are shown in Table 4 and Figure 12; changes in w are smaller than the statistical uncertainty of $\lesssim 0.03$ given in the full Pantheon+ w measurement from Brout et al. (2022) and the uncertainty of 0.04 from Pantheon (Scolnic et al. 2018). Applying all updates to the original redshifts results in $\Delta w = 0.003$. The largest redshift variations, that is shifting all redshifts by their 1σ uncertainties (variations 8 and 9) result in $|\Delta w| \leq 0.015$.

7.4 SN- z vs host- z

Using the original Pantheon sample, Steinhardt et al. (2020) find a statistically significant shift in the cosmological parameters derived for the subset of SNe that have redshifts measured from the supernova (SN- z) and those that have host-galaxy redshifts (host- z). Here we revisit this analysis with our updated data.

There are several important differences between Steinhardt et al. (2020) and our analysis: (1) Steinhardt et al. (2020) fit all w CDM parameters simultaneously, (2) our definition of the SN- z sample is stricter than their not-host- z , in that we allow host emission-lines in SN-dominated spectra to be assigned to the host- z sample, and (3) our allocation of SN- z particularly for PS1MD and SDSS SNe differs from theirs. We expect the SDSS classifications to differ because, as we addressed in Section 3, we updated 81 SN- z s to host- z s (and further, applied the $+2.2 \times 10^{-3}$ systematic offset to the remaining SN- z s as determined in Sako et al. 2018). However, the reason for the PS1MD classification differences are unclear; our classifications come directly from reported redshift uncertainties (SN- z have uncertainties of 0.01 and host- z 0.001).

We find that restricting the data to only those SNe with host- z (variation 6 in Table 4 and Figure 12) gives $\Delta H_0 = 0.05 \pm 0.20 \text{ km s}^{-1} \text{ Mpc}^{-1}$ (i.e. 0.3σ) relative to the nominal Final dataset. By contrast, when we restrict the data to the SN- z sample (of

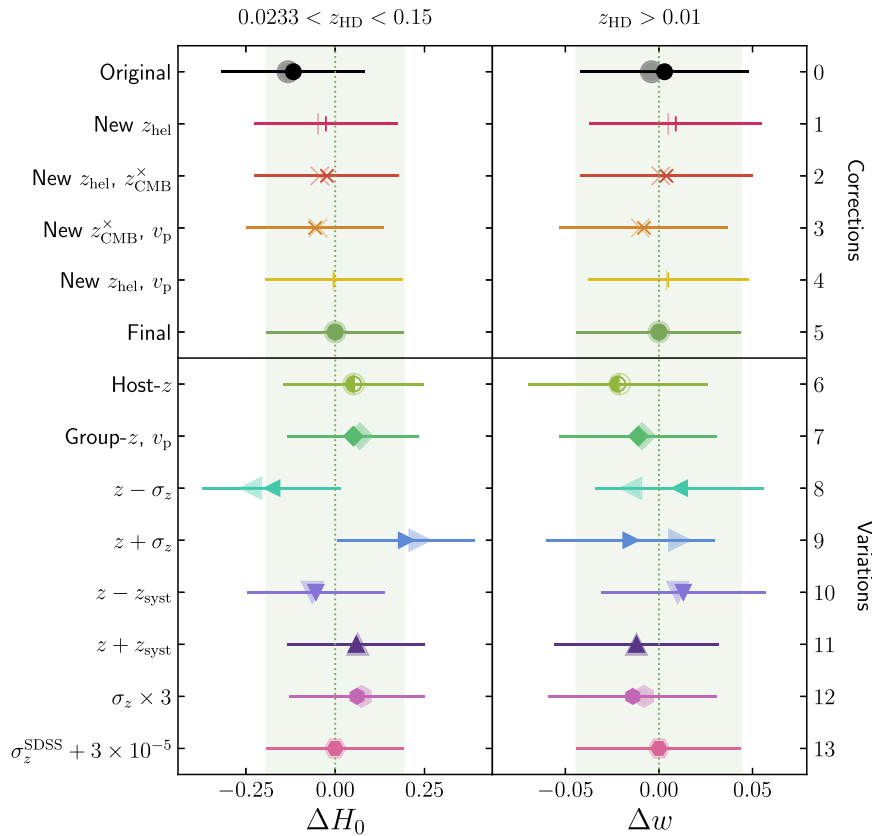


Figure 12. The impact on inferences of H_0 and w due to changes in the redshifts. The regular symbols are the nominal results while the faint, larger symbols come from recalculating μ after changing redshift so that the partial cancellations seen in Figure 11 are not present. The descriptions on the left hand side and variation numbers on the right hand side both correspond to the descriptions in Table 4. The H_0 fit uses the redshift range $0.0233 < z_{HD} < 0.15$, while the w fit uses the range $z_{HD} > 0.01$, where the maximum redshift of the sample is 2.26. The uncertainties in both H_0 and w only represent the statistical uncertainty from the SN magnitude uncertainties—they do not contain any uncertainty from distance ladder calibration nor intrinsic dispersion in SN magnitudes. All variations are small, showing that the cosmology results are robust to small changes in redshift and there is no indication of systematic redshift errors biasing previous results.

which only 17 are in the redshift range of the H_0 fit, we find $\Delta H_0 = -2.8 \pm 1.3 \text{ km s}^{-1} \text{ Mpc}^{-1}$.

These results are broadly consistent with Steinhardt et al. (2020), who found that $\Delta H_0 = 0.45 \pm 0.25 \text{ km s}^{-1} \text{ Mpc}^{-1}$ for the host- z sample and $\Delta H_0 = -0.96 \pm 0.50 \text{ km s}^{-1} \text{ Mpc}^{-1}$ for the SN- z sample. The significance of the shift in the host- z sample is lower in our case, which is likely due to the greater proportion of host- z redshifts in our sample and the corrections we have implemented to the SN- z based on the systematic offset correction determined by Sako et al. (2018). On the other hand, the H_0 shift we find in the SN- z sample is larger than Steinhardt et al. (2020), but our results are of similar significance (approximately 2σ in each case) since we have fewer SNe in the SN- z sample.

Increasing the redshift range over which we fit for H_0 adds some model dependence, but allows us to include more of the SN- z sample. When we do so the deviation from the nominal dataset vanishes, with the results from SN- z alone agreeing with the result from host- z alone (within 1σ) for all $z_{max} \gtrsim 0.25$. Figure 13 shows the impact of including or excluding SN- z from our fit for H_0 , as a function of redshift range used in the fit. The impact is small, with $|\Delta H_0| \lesssim 0.05 \text{ km s}^{-1} \text{ Mpc}^{-1}$.

As expected, Figure 13 shows that as we increase the maximum redshift in our H_0 fit the cosmological model-dependence becomes increasingly apparent. The $v_{approx}(z, q_0, j_0)$ equation in

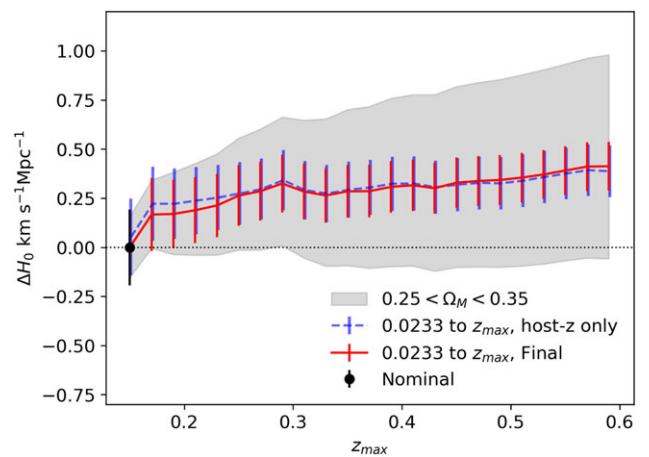


Figure 13. The dependence of H_0 on the redshift-range we fit over. The horizontal axis shows the maximum redshift used in the fit, keeping the minimum redshift as $z_{HD} = 0.0233$. Red shows the Final sample, and blue shows the host- z sample in order to demonstrate the impact of excluding SNe that only have SN- z . As redshift increases the cosmological model dependence becomes increasingly important so the grey shading shows the range of H_0 values from fitting with $0.25 < \Omega_m < 0.35$ in the flat- Λ CDM model ($\Omega_m = 0.35$ being the lower edge). At the nominal upper redshift limit of $z_{max} = 0.15$ the statistical variance of the sample (black error bar) remains larger than the uncertainty due to even this quite wide range of Ω_m .

Section 7.2 is a good approximation to the full equation $v(z) = c \int_0^z \frac{dz}{E(z)}$ where $E(z) \equiv H(z)/H_0$, as long as $\Omega_m \sim 0.3$ for the flat- Λ CDM model. Over the nominal redshift range of $0.0233 < z_{\text{HD}} < 0.15$ (black point) a shift of $\Delta\Omega_m \pm 0.05$ results in $\Delta H_0 \mp 0.2 \text{ km s}^{-1} \text{ Mpc}^{-1}$, showing the cosmological model-dependence is still sub-dominant to the sampling uncertainties on H_0 (which is the purpose of using the restricted redshift range).

For the equation of state of dark energy, the host- z only case (6) shows a shift of $\Delta w = -0.022 \pm 0.048$. This is the largest impact on w of any variation, albeit still insignificant (0.6σ). Using only SN- z gives $\Delta w = 0.25 \pm 0.16$. The reason for this shift can be seen in Figure 10, where the SN- z sample shows a systematic positive offset in $\Delta\mu$ at low redshift, but a negative offset at high redshift. Any shift with a redshift dependence will have an impact on w whereas a constant shift would mainly affect H_0 .

Given these results, in Section 8 we discuss whether SN- z samples should be included in cosmological fits.

7.5 Redshift systematics and uncertainty values

As expected, some of the largest changes in H_0 and w occur when we add a systematic shift to all redshifts in the sample (variations 8–11). However, even when we shift the redshifts systematically by their uncertainties (variations 8–9) the impact is only $|\Delta H_0| \sim 0.2 \pm 0.2 \text{ km s}^{-1} \text{ Mpc}^{-1}$ and $|\Delta w| \sim 0.015 \pm 0.045$, smaller than the sample uncertainties in each case.

Changing the size of the uncertainties on the redshifts has a negligible impact on the cosmological parameters (variations 12–13).

8. Discussion and conclusions

Motivated in part by the fact that a systematic error in redshift could affect standard candle derivations of H_0 , especially if it were at low redshift, we have reviewed and revised the redshifts for the Pantheon+ supernova sample. This includes fixing bookkeeping errors, updating heliocentric redshifts when available, adding uncertainty estimates, converting from the heliocentric to the CMB-frame redshifts without using the low- z additive approximation, updating peculiar velocity estimates at all redshifts, and correcting the peculiar velocities from large-scale flow predictions at large redshifts.

These curated redshifts are the ones that should be used in the future for all supernova cosmology analyses using these data. They are available at the CDS VizieR database and also <https://github.com/PantheonPlusSH0ES/DataRelease>, and the code that generated the peculiar velocity predictions can be found at <https://github.com/KSaid-1/pvhub>.

We found that these redshift updates do not have a large impact on cosmological results. This fortunate circumstance arises for a few reasons. Firstly, errors at high- z are relatively unimportant, because the relative uncertainty in redshift decreases as redshift increases. That is compounded by the fact that a particular Δz corresponds to a much smaller *distance* difference at high- z than at low- z . Furthermore the $\Delta\mu$ versus Δz correlation we mentioned in Section 7.1 and Figure 11 reduces the impact of redshift errors, especially near $z \sim 0.5$. Thus at high- z even a large error in redshift gives a small error in expected magnitude.

Secondly, for the SNe at very low redshifts ($z < 0.01$) that are used to calibrate the SN Ia absolute magnitude, the redshifts are

not used—they are replaced by the brightness of another standard candle (TRGB or Cepheids), that acts as an anchor.

Finally, many potential systematic redshift errors (for example due to the approximate heliocentric to CMB-frame conversion) are only systematic if the sample covers a small area of the sky. The low- z supernova sample ($z \lesssim 0.15$), for which redshift errors could have a large impact, is spread across most of the sky (see Figure 1). We also confirmed in Section 6.1 that the new peculiar velocities do not *systematically* differ from those previously predicted. Thus the updates to the redshifts of Pantheon+ mostly caused random shifts, predominantly via updating z_{hel} and v_p . Across the whole sample the root-mean-square deviation of all the redshift changes was $\sim 3 \times 10^{-3}$, however the mean redshift change was an order of magnitude smaller ($\sim 4 \times 10^{-4}$). Within the redshift range $0.0233 < z_{\text{HD}} < 0.15$, $\text{RMS}(\Delta z_{\text{HD}}) \sim 1 \times 10^{-3}$ and the mean redshift change was $\sim 1 \times 10^{-4}$. The mean change is actually almost completely frame and redshift-range independent, but is smaller for the H_0 sample because, unlike for the mean z_{hel} of the full sample, it does not account for repeat observations of the same SNe originally being assigned different z_{hel} . This resulting impact on H_0 is consistent with that predicted by (Davis *et al.* 2019, see the green dashed line in their Figure 4).

We compared the cosmological results with and without the sample that has only supernova redshifts in Section 7.4). As in previous studies (e.g. Steinhardt *et al.* 2020), we found differences in the results from these sub-samples, the most significant of which was a 2σ deviation in H_0 for the SN- z sub-sample. While it is possible this is a statistical fluctuation with so few SNe in the SN- z sample, there are reasons to expect a systematic offset from the host- z sample. When host galaxies lack redshifts it is usually because they are faint and/or low-mass, and SNe Ia properties are correlated with their hosts' properties (e.g. Sullivan *et al.* 2006; Smith *et al.* 2020b; Wiseman *et al.* 2020). Therefore the SN- z sample could represent a physically different subset of SNe that is not accounted for in, for example, SALT2 modelling. Alternatively, a slight bias could arise if, for example, supernova spectral templates do not fully account for the blueshift due to the velocity of the visible side of the supernova's photosphere.

Given the greater uncertainty in supernova redshifts compared to host-galaxy redshifts, and the potential for bias (as seen with SDSS SNe in Zheng *et al.* 2008; Sako *et al.* 2018), one could consider removing all supernovae that lack a host redshift from cosmology samples. This would reduce the cosmologically useful sample size slightly, and thus sacrifice a small amount of precision for potentially greater accuracy. At $z < 0.15$ approximately 3% of the Type Ia supernova sample lacks host galaxy redshifts, but that proportion increases to approximately 10% at high redshift. Excluding the SN- z excludes a different proportion of the supernova population as a function of redshift. While this effect should be monitored for future cosmological studies (and should motivate further follow-up efforts to get host- z), we have shown here that the impact of including or excluding the SN- z sample remains small relative to the uncertainties in the measurement (Figure 13).

Finally, we have also made sure all supernova redshifts now have estimated uncertainties. As noted by Steinhardt *et al.* (2020), uncertainties are important because sampling from a symmetric redshift uncertainty systematically prefers a larger μ for a given redshift due to the sublinear nature of the $\mu(z)$ relation. This would effectively reduce the gradient of the $\mu(z)$ relation at low- z and cause samples with large uncertainties (such SN- z) to prefer a smaller H_0 . Furthermore, the precision of redshift indirectly

affects one of the largest systematic uncertainties in SNe Ia analyses: the determination of their intrinsic scatter. If the precision is not correctly measured, more or less scatter will be attributed to the intrinsic variation of SN Ia distances, which could bias the modelling used to determine accurate distances. Additionally, the precision and accuracy of redshifts must be known accurately when using SNe Ia to measure growth-of-structure. In that case, instead of applying peculiar velocities to SNe from an external model, one uses SNe Ia to measure peculiar velocities.

Most of the uncertainties we provide are based on the precision of a particular survey or sample. A better method for determining uncertainties would be to estimate them on a spectrum-by-spectrum basis. However, we tested the impact of changing the uncertainties (see Figure 12) and it had a negligible effect on the cosmological results, so we conclude that the uncertainties we provide are sufficient for current data.

While new surveys and datasets will continue to come online over the next decade, the sample presented here will not easily be replaced due to its utility for measuring H_0 , which is rate-limited by the number of SNe in the very-nearby universe and will take another 30 yr to re-accumulate. Because of that importance, in this work we endeavour to provide an updated and homogeneously treated set of supernova redshifts that we hope will be useful to the community.

Acknowledgement. The authors thank A. Whitford, C. Chang, Y. Lai, A. Glanville and L. Rauf for assisting in visual inspection of host galaxies and performing redshift checks in NED (Section 3). We also thank C. Howlett, M. Colless, and M. Hudson for useful discussions on peculiar velocities and M. Smith for insights into SN host galaxies. TMD is the recipient of an Australian Research Council Australian Laureate Fellowship (project number FL180100168) funded by the Australian Government. DS is supported by DOE grant DE-SC0010007, DE-SC0021962 and the David and Lucile Packard Foundation. DS is supported in part by the National Aeronautics and Space Administration under Contract No. NNG17PX03C issued through the Roman Science Investigation Teams Programme.

This work has made use of the NASA/IPAC Extragalactic Database, which is funded by the National Aeronautics and Space Administration and operated by the California Institute of Technology. This work was also supported by resources provided by the University of Chicago Research Computing Center, and based in part on data acquired at the Anglo-Australian Telescope. We acknowledge the traditional custodians of the land on which the AAT stands, the Gamilaraay people, and pay our respects to elders past and present.

References

- Abazajian, K. N., et al. 2009, *ApJS*, **182**, 543
 Balam, D. 2016, *TNSCR*, **2016-48**, 1
 Bassett, B., et al. 2006, *CBET*, **743**, 1
 Bassett, B., et al. 2007, *CBET*, **1102**, 1
 Betoule, M., et al. 2014, *A&A*, **568**, A22
 Blondin, S., Modjaz, M., Kirshner, R., Challis, P., & Calkins, M. 2007, *Central Bureau Electronic Telegrams*, **978**, 1
 Blondin, S., & Tonry, J. L. 2007, *ApJ*, **666**, 1024
 Blondin, S., et al. 2012, *AJ*, **143**, 126
 Bolton, A. S., et al. 2012, *AJ*, **144**, 144
 Bonnarel, F., et al. 2000, *A&AS*, **143**, 33
 Boruah, S. S., Hudson, M. J., & Lavaux, G. 2020, *MNRAS*, **498**, 2703
 Bosma, A., & Freeman, K. C. 1993, *AJ*, **106**, 1394
 Brout, D., et al. 2019, *ApJ*, **874**, 150
 Brout, D., et al. 2021, arXiv e-prints, p. arXiv:2112.03864
 Brout, D., et al. 2022, arXiv e-prints, p. arXiv:2202.04077
 Brown, P. J., Breeveld, A. A., Holland, S., Kuin, P., & Pritchard, T. 2014, *Ap&SS*, **354**, 89
 Burns, C. R., et al. 2018, *ApJ*, **869**, 56
 Burns, C. R., et al. 2020, *ApJ*, **895**, 118
 Calcino, J., & Davis, T. 2017, *JCAP*, **2017**, 038
 Carr, A., & Davis, T. 2021, *ApJ*, **914**, 97
 Carrick, J., Turnbull, S. J., Lavaux, G., & Hudson, M. J. 2015, *MNRAS*, **450**, 317
 Chen, P., et al. 2020, arXiv e-prints, p. arXiv:2011.02461
 Chen, R., et al. 2022, arXiv e-prints, p. arXiv:2202.10480
 Childress, M., et al. 2013, *ApJ*, **770**, 107
 Colless, M., et al. 2001, *MNRAS*, **328**, 1039
 Colless, M., et al. 2003, arXiv e-prints, pp astro-ph/0306581
 Contreras, C., et al. 2010, *AJ*, **139**, 519
 Dark Energy Survey. 2019, *ApJ*, **872**, L30
 Davis, T. M., Hinton, S. R., Howlett, C., & Calcino, J. 2019, *MNRAS*, **490**, 2948
 de Vaucouleurs, G., de Vaucouleurs, A., Corwin Herold, G. J., Buta, R. J., Paturel, G., & Fouque, P. 1991, *Third Reference Catalogue of Bright Galaxies* (New York: Springer-Verlag)
 Drinkwater, M. J., et al. 2018, *MNRAS*, **474**, 4151
 Falco, E. E., et al. 1999, *PASP*, **111**, 438
 Filippenko, A. V., Wong, D. S., & Ganeshalingam, M. 2007, *CBET*, **984**, 1
 Fixsen, D. J., Cheng, E. S., Gales, J. M., Mather, J. C., Shafer, R. A., & Wright, E. L. 1996, *ApJ*, **473**, 576
 Folatelli, G., et al. 2013, *ApJ*, **773**, 53
 Foley, R. J., et al. 2018, *MNRAS*, **475**, 193
 Fouqué, P., Durand, N., Bottinelli, L., Gouguenheim, L., & Paturel, G. 1992, *Catalogue of Optical Radial Velocities. Monographies de la base de données extragalactiques*, Observatoire de Lyon
 Gall, C., et al. 2018, *A&A*, **611**, A58
 Ganeshalingam, M., et al. 2010, *ApJS*, **190**, 418
 Garnavich, P., Marion, H., Challis, P., Blondin, S., & Kirshner, R. 2007, *CBET*, **1176**, 1
 Gilliland, R. L., Nugent, P. E., & Phillips, M. M. 1999, *ApJ*, **521**, 30
 Goldhaber, G., et al. 2001, *ApJ*, **558**, 359
 Gupta, R. R., et al. 2011, *ApJ*, **740**, 92
 Gupta, R. R., et al. 2016, *AJ*, **152**, 154
 Guy, J., et al. 2007, *A&A*, **466**, 11
 Guy, J., et al. 2010, *A&A*, **523**, A7
 Hamuy, M., et al. 1996, *AJ*, **112**, 2408
 Hicken, M., et al. 2009, *ApJ*, **700**, 331
 Hicken, M., et al. 2012, *ApJS*, **200**, 12
 Hinton, S., & Brout, D. 2020, *JOSS*, **5**, 2122
 Hsiao, E. Y., et al. 2015, *A&A*, **578**, A9
 Huchra, J., et al. 2005, in *Astronomical Society of the Pacific Conference Series*, Vol. 329, *Nearby Large-Scale Structures and the Zone of Avoidance*, ed. A. P. Fairall, & P. A. Woudt, 135
 Huchra, J. P., Vogeley, M. S., & Geller, M. J. 1999, *ApJS*, **121**, 287
 Huchra, J. P., et al. 2012, *ApJS*, **199**, 26
 Huterer, D., Kim, A., Krauss, L. M., & Broderick, T. 2004, *ApJ*, **615**, 595
 Jha, S., et al. 2006, *AJ*, **131**, 527
 Jha, S., Riess, A. G., & Kirshner R. P. 2007, *ApJ*, **659**, 122
 Jones, D. H., et al. 2009, *MNRAS*, **399**, 683
 Jørgensen, I., Chiboucas, K., Webb, K., & Woodrum, C. 2018, *AJ*, **156**, 224
 Kawabata, M., et al. 2020, *ApJ*, **893**, 143
 Kessler, R., & Scolnic, D. 2017, *ApJ*, **836**, 56
 Kessler, R., et al. 2009, *PASP*, **121**, 1028
 Kessler, R., et al. 2019, *MNRAS*, **485**, 1171
 Kiyota, S., et al. 2014, *ATel*, **6809**, 1
 Krisciunas, K., Suntzeff, N. B., Espinoza, J., Gonzalez, D., Miranda, A., & Sanhueza, P. 2017a, *RNAAS*, **1**, 36
 Krisciunas, K., et al. 2017b, *AJ*, **154**, 211
 Lahav, O., Santiago, B. X., Webster, A. M., Strauss, M. A., Davis, M., Dressler, A., & Huchra, J. P. 2000, *MNRAS*, **312**, 166
 Lasker, J., et al. 2019, *MNRAS*, **485**, 5329
 Lavaux, G., & Hudson, M. J. 2011, *MNRAS*, **416**, 2840

- Li, W., Filippenko, A. V., Treffers, R. R., Riess, A. G., Hu, J., & Qiu, Y. 2001, *ApJ*, **546**, 734
- Lidman, C., et al. 2020, *MNRAS*, **496**, 19
- Matheson, T., Challis, P., Kirshner, R., Macri, L., & Berlind, P. 2002, *IAU Circ.*, **8013**, 2
- Milne, P. A., et al. 2010, *ApJ*, **721**, 1627
- Mitra, A., & Linder, E. V. 2021, *PhRvD*, **103**, 023524
- Mueller, J., Rykoski, K. M., Garnavich, P., Riess, A., Kirshner, R., Luu, J., & Koranyi, D. 1996, *IAUC*, **6317**, 1
- Nakano, S., et al. 2010, *CBET*, **2200**, 1
- Östman, L., et al. 2011, *A&A*, **526**, A28
- Perlmutter, S., et al. 1999, *ApJ*, **517**, 565
- Peterson, E. R., et al. 2021, arXiv e-prints, p. arXiv:2110.03487
- Phillips, M. M. 1993, *ApJ*, **413**, L105
- Phillips, M. M., Lira, P., Suntzeff, N. B., Schommer, R. A., Hamuy, M., & Maza, J. 1999, *AJ*, **118**, 1766
- Phillips, M. M., et al. 2019, *PASP*, **131**, 014001
- PLANCK Collaboration, et al. 2020, *A&A*, **641**, A1
- Quimby, R., Madison, D. R., Li, W., Shetrone, M., & Riley, V. 2007, *CBET*, **873**, 1
- Rameez, M., & Sarkar, S. 2021, *CQG*, **38**, 154005
- Riess, A. G., et al. 1998, *AJ*, **116**, 1009
- Riess, A. G., et al. 1999, *AJ*, **117**, 707
- Riess, A. G., et al. 2001, *ApJ*, **560**, 49
- Riess, A. G., et al. 2004, *ApJ*, **607**, 665
- Riess, A. G., et al. 2007, *ApJ*, **659**, 98
- Riess, A. G., et al. 2016, *ApJ*, **826**, 56
- Riess, A. G., et al. 2018, *ApJ*, **853**, 126
- Riess, A. G., et al. 2022, *ApJ*, **934**, L7
- Said, K., Colless, M., Magoulas, C., Lucey, J. R., & Hudson, M. J. 2020, *MNRAS*, **497**, 1275
- Sako, M., et al., 2018, *PASP*, **130**, 064002
- Scolnic, D., et al. 2015, *ApJ*, **815**, 117
- Scolnic, D., et al. 2021, arXiv e-prints, p. arXiv:2112.03863
- Scolnic, D. M., et al. 2018, *ApJ*, **859**, 101
- Silverman, J. M., et al. 2012, *MNRAS*, **425**, 1789
- Smith, M., et al. 2020a, *AJ*, **160**, 267
- Smith, M., et al. 2020b, *MNRAS*, **494**, 4426
- Springob, C. M., Haynes, M. P., Giovanelli, R., & Kent B. R. 2005, *ApJS*, **160**, 149
- Stahl, B. E., et al. 2019, *MNRAS*, **490**, 3882
- Steinhardt, C. L., Sneppen, A., & Sen, B. 2020, *ApJ*, **902**, 14
- Stritzinger, M., et al. 2010, *AJ*, **140**, 2036
- Sullivan, M., et al. 2006, *ApJ*, **648**, 868
- Suzuki, N., et al. 2012, *ApJ*, **746**, 85
- Theureau, G., Bottinelli, L., Coudreau-Durand, N., Gougouenheim, L., Hallet, N., Loulergue, M., Patrel, G., & Teerikorpi, P. 1998, *A&AS*, **130**, 333
- Tonry, J., & Davis, M. 1979, *AJ*, **84**, 1511
- Tripp, R. 1998, *A&A*, **331**, 815
- Tsvetkov, D. Y., & Elenin, L. 2010, *PZ*, **30**, 2
- van den Bosch, R. C. E., Gebhardt, K., Gültekin, K., Yldrm, A., & Walsh, J. L. 2015, *ApJS*, **218**, 10
- Wang, L., Baade, D., Clocchiatti, A., Maund, J., Patat, F., & Quinn, J. 2008, *CBET*, **1509**, 1
- Wang, L., Pulliam, C., & Wheeler, J. C. 1997, *IAUC*, **6753**, 2
- Wee, J., Chakraborty, N., Wang, J., & Penprase, B. E. 2018, *ApJ*, **863**, 90
- Wegner, G., et al. 2003, *AJ*, **126**, 2268
- Wiseman, P., et al. 2020, *MNRAS*, **495**, 4040
- Wojtak, R., Davis, T. M., & Wiis, J. 2015, *JCAP*, **2015**, 025
- Wood-Vasey, W. M., et al. 2007, *ApJ*, **666**, 694
- Yan, P.-F., Yuan, Q.-R., Zhang, L., & Zhou, X. 2014, *AJ*, **147**, 106
- Yuan, F., Quimby, R., Sisson, M. D., Chamorro, D., Akerlof, C., & Wheeler, J. C. 2008a, *CBET*, **1245**, 1
- Yuan, F., et al. 2008b, *CBET*, **1513**, 1
- Yuk, H., Zheng, W., Filippenko, A. V., Masi, G., Balam, D. D., Graham, M. L., & Hsiao, E. Y. 2014, *CBET*, **3893**, 1
- Zhang, J., & Wang, X. 2014, *ATel*, **6171**, 1
- Zhang, T., et al. 2010, *PASP*, **122**, 1
- Zheng, C., et al. 2008, *AJ*, **135**, 1766

Appendix A. Supplementary Data Tables

Table A1. Averaging of multiple SDSS redshifts.

SNID	Host	z_{hel}	σ_z	\bar{z}	$\sigma_{\bar{z}}$																																												
2003cq	NGC 3978	0.033176	1.0×10^{-5}	0.033194	1.8×10^{-5}																																												
		0.033211	1.2×10^{-5}			2003du	UGC 9391	0.006352	1.2×10^{-5}	0.006377	1.6×10^{-5}	0.006373	1.2×10^{-5}	0.006406	1.3×10^{-5}	2003Y	IC 0522	0.016897	0.5×10^{-5}	0.016892	1.2×10^{-5}	0.016923	0.7×10^{-5}	0.016865	0.7×10^{-5}	0.016884	0.8×10^{-5}	1580	WISEA J030117.99-003842.4	0.182908	2.3×10^{-5}	0.182932	1.2×10^{-5}	0.182944	1.9×10^{-5}	0.182945	1.9×10^{-5}	2005eq	MCG -01-09-006	0.028907	1.0×10^{-5}	0.028952	4.5×10^{-5}	0.028996	1.0×10^{-5}	13655	WISEA J023605.02-005939.8	0.262757	5.2×10^{-5}
2003du	UGC 9391	0.006352	1.2×10^{-5}	0.006377	1.6×10^{-5}																																												
		0.006373	1.2×10^{-5}																																														
		0.006406	1.3×10^{-5}			2003Y	IC 0522	0.016897	0.5×10^{-5}	0.016892	1.2×10^{-5}	0.016923	0.7×10^{-5}	0.016865	0.7×10^{-5}			0.016884	0.8×10^{-5}			1580	WISEA J030117.99-003842.4	0.182908	2.3×10^{-5}	0.182932	1.2×10^{-5}	0.182944	1.9×10^{-5}	0.182945	1.9×10^{-5}	2005eq	MCG -01-09-006	0.028907	1.0×10^{-5}	0.028952	4.5×10^{-5}	0.028996	1.0×10^{-5}	13655	WISEA J023605.02-005939.8	0.262757	5.2×10^{-5}	0.262699	5.9×10^{-5}	0.262640	3.9×10^{-5}		
2003Y	IC 0522	0.016897	0.5×10^{-5}	0.016892	1.2×10^{-5}																																												
		0.016923	0.7×10^{-5}																																														
		0.016865	0.7×10^{-5}																																														
		0.016884	0.8×10^{-5}			1580	WISEA J030117.99-003842.4	0.182908	2.3×10^{-5}	0.182932	1.2×10^{-5}	0.182944	1.9×10^{-5}	0.182945	1.9×10^{-5}	2005eq	MCG -01-09-006	0.028907	1.0×10^{-5}	0.028952	4.5×10^{-5}	0.028996	1.0×10^{-5}	13655	WISEA J023605.02-005939.8	0.262757	5.2×10^{-5}	0.262699	5.9×10^{-5}	0.262640	3.9×10^{-5}																		
1580	WISEA J030117.99-003842.4	0.182908	2.3×10^{-5}	0.182932	1.2×10^{-5}																																												
		0.182944	1.9×10^{-5}																																														
		0.182945	1.9×10^{-5}			2005eq	MCG -01-09-006	0.028907	1.0×10^{-5}	0.028952	4.5×10^{-5}	0.028996	1.0×10^{-5}	13655	WISEA J023605.02-005939.8	0.262757	5.2×10^{-5}	0.262699	5.9×10^{-5}	0.262640	3.9×10^{-5}																												
2005eq	MCG -01-09-006	0.028907	1.0×10^{-5}	0.028952	4.5×10^{-5}																																												
		0.028996	1.0×10^{-5}			13655	WISEA J023605.02-005939.8	0.262757	5.2×10^{-5}	0.262699	5.9×10^{-5}	0.262640	3.9×10^{-5}																																				
13655	WISEA J023605.02-005939.8	0.262757	5.2×10^{-5}	0.262699	5.9×10^{-5}																																												
		0.262640	3.9×10^{-5}																																														

Table A1. Continued.

SNID	Host	z_{hel}	σ_z	\bar{z}	$\sigma_{\bar{z}}$																																																																																						
2006ccq	IC 4239	0.048475	1.2×10^{-5}	0.048442	3.3×10^{-5}																																																																																						
		0.048409	1.2×10^{-5}			18809	WISEA J032331.35+004002.1	0.132185	3.7×10^{-5}	0.132159	2.6×10^{-5}	0.132133	3.5×10^{-5}	20039	WISEA J003931.06+010125.2	0.246696	2.7×10^{-5}	0.246809	5.7×10^{-5}	0.246882	2.5×10^{-5}	0.246850	2.2×10^{-5}	2007su	SDSS J221908.85+131040.4	0.027821	0.6×10^{-5}	0.027832	1.1×10^{-5}	0.027842	0.6×10^{-5}	2008ac	J115345.22+482521.0	0.052828	4.6×10^{-5}	0.052808	2.0×10^{-5}	0.052788	8.2×10^{-5}	2008ds	UGC 299	0.021054	1.0×10^{-5}	0.021061	0.7×10^{-5}	0.021068	1.2×10^{-5}	2010A	UGC 2019	0.020745	1.2×10^{-5}	0.020755	1.0×10^{-5}	0.020765	1.4×10^{-5}	2010ag	UGC 10679	0.033690	1.1×10^{-5}	0.033715	2.5×10^{-5}	0.033739	1.2×10^{-5}	2010ai	WISEA J125925.01+275948.2	0.018282	2.6×10^{-5}	0.018267	1.5×10^{-5}	0.018252	3.5×10^{-5}	590194	WISEA J084056.86+443127.4	0.089493	1.3×10^{-5}	0.089513	2.0×10^{-5}	0.089532	1.3×10^{-5}	2011im	NGC 7364	0.016161	0.6×10^{-5}	0.016163	0.2×10^{-5}	0.016164	0.8×10^{-5}	2013gs	UGC 5066	0.016797	1.6×10^{-5}
18809	WISEA J032331.35+004002.1	0.132185	3.7×10^{-5}	0.132159	2.6×10^{-5}																																																																																						
		0.132133	3.5×10^{-5}			20039	WISEA J003931.06+010125.2	0.246696	2.7×10^{-5}	0.246809	5.7×10^{-5}	0.246882	2.5×10^{-5}			0.246850	2.2×10^{-5}			2007su	SDSS J221908.85+131040.4	0.027821	0.6×10^{-5}	0.027832	1.1×10^{-5}	0.027842	0.6×10^{-5}	2008ac	J115345.22+482521.0	0.052828	4.6×10^{-5}	0.052808	2.0×10^{-5}	0.052788	8.2×10^{-5}	2008ds	UGC 299	0.021054	1.0×10^{-5}	0.021061	0.7×10^{-5}	0.021068	1.2×10^{-5}	2010A	UGC 2019	0.020745	1.2×10^{-5}	0.020755	1.0×10^{-5}	0.020765	1.4×10^{-5}	2010ag	UGC 10679	0.033690	1.1×10^{-5}	0.033715	2.5×10^{-5}	0.033739	1.2×10^{-5}	2010ai	WISEA J125925.01+275948.2	0.018282	2.6×10^{-5}	0.018267	1.5×10^{-5}	0.018252	3.5×10^{-5}	590194	WISEA J084056.86+443127.4	0.089493	1.3×10^{-5}	0.089513	2.0×10^{-5}	0.089532	1.3×10^{-5}	2011im	NGC 7364	0.016161	0.6×10^{-5}	0.016163	0.2×10^{-5}	0.016164	0.8×10^{-5}	2013gs	UGC 5066	0.016797	1.6×10^{-5}	0.016812	1.5×10^{-5}	0.016827	1.7×10^{-5}
20039	WISEA J003931.06+010125.2	0.246696	2.7×10^{-5}	0.246809	5.7×10^{-5}																																																																																						
		0.246882	2.5×10^{-5}																																																																																								
		0.246850	2.2×10^{-5}			2007su	SDSS J221908.85+131040.4	0.027821	0.6×10^{-5}	0.027832	1.1×10^{-5}	0.027842	0.6×10^{-5}	2008ac	J115345.22+482521.0	0.052828	4.6×10^{-5}	0.052808	2.0×10^{-5}	0.052788	8.2×10^{-5}	2008ds	UGC 299	0.021054	1.0×10^{-5}	0.021061	0.7×10^{-5}	0.021068	1.2×10^{-5}	2010A	UGC 2019	0.020745	1.2×10^{-5}	0.020755	1.0×10^{-5}	0.020765	1.4×10^{-5}	2010ag	UGC 10679	0.033690	1.1×10^{-5}	0.033715	2.5×10^{-5}	0.033739	1.2×10^{-5}	2010ai	WISEA J125925.01+275948.2	0.018282	2.6×10^{-5}	0.018267	1.5×10^{-5}	0.018252	3.5×10^{-5}	590194	WISEA J084056.86+443127.4	0.089493	1.3×10^{-5}	0.089513	2.0×10^{-5}	0.089532	1.3×10^{-5}	2011im	NGC 7364	0.016161	0.6×10^{-5}	0.016163	0.2×10^{-5}	0.016164	0.8×10^{-5}	2013gs	UGC 5066	0.016797	1.6×10^{-5}	0.016812	1.5×10^{-5}	0.016827	1.7×10^{-5}														
2007su	SDSS J221908.85+131040.4	0.027821	0.6×10^{-5}	0.027832	1.1×10^{-5}																																																																																						
		0.027842	0.6×10^{-5}			2008ac	J115345.22+482521.0	0.052828	4.6×10^{-5}	0.052808	2.0×10^{-5}	0.052788	8.2×10^{-5}	2008ds	UGC 299	0.021054	1.0×10^{-5}	0.021061	0.7×10^{-5}	0.021068	1.2×10^{-5}	2010A	UGC 2019	0.020745	1.2×10^{-5}	0.020755	1.0×10^{-5}	0.020765	1.4×10^{-5}	2010ag	UGC 10679	0.033690	1.1×10^{-5}	0.033715	2.5×10^{-5}	0.033739	1.2×10^{-5}	2010ai	WISEA J125925.01+275948.2	0.018282	2.6×10^{-5}	0.018267	1.5×10^{-5}	0.018252	3.5×10^{-5}	590194	WISEA J084056.86+443127.4	0.089493	1.3×10^{-5}	0.089513	2.0×10^{-5}	0.089532	1.3×10^{-5}	2011im	NGC 7364	0.016161	0.6×10^{-5}	0.016163	0.2×10^{-5}	0.016164	0.8×10^{-5}	2013gs	UGC 5066	0.016797	1.6×10^{-5}	0.016812	1.5×10^{-5}	0.016827	1.7×10^{-5}																						
2008ac	J115345.22+482521.0	0.052828	4.6×10^{-5}	0.052808	2.0×10^{-5}																																																																																						
		0.052788	8.2×10^{-5}			2008ds	UGC 299	0.021054	1.0×10^{-5}	0.021061	0.7×10^{-5}	0.021068	1.2×10^{-5}	2010A	UGC 2019	0.020745	1.2×10^{-5}	0.020755	1.0×10^{-5}	0.020765	1.4×10^{-5}	2010ag	UGC 10679	0.033690	1.1×10^{-5}	0.033715	2.5×10^{-5}	0.033739	1.2×10^{-5}	2010ai	WISEA J125925.01+275948.2	0.018282	2.6×10^{-5}	0.018267	1.5×10^{-5}	0.018252	3.5×10^{-5}	590194	WISEA J084056.86+443127.4	0.089493	1.3×10^{-5}	0.089513	2.0×10^{-5}	0.089532	1.3×10^{-5}	2011im	NGC 7364	0.016161	0.6×10^{-5}	0.016163	0.2×10^{-5}	0.016164	0.8×10^{-5}	2013gs	UGC 5066	0.016797	1.6×10^{-5}	0.016812	1.5×10^{-5}	0.016827	1.7×10^{-5}																														
2008ds	UGC 299	0.021054	1.0×10^{-5}	0.021061	0.7×10^{-5}																																																																																						
		0.021068	1.2×10^{-5}			2010A	UGC 2019	0.020745	1.2×10^{-5}	0.020755	1.0×10^{-5}	0.020765	1.4×10^{-5}	2010ag	UGC 10679	0.033690	1.1×10^{-5}	0.033715	2.5×10^{-5}	0.033739	1.2×10^{-5}	2010ai	WISEA J125925.01+275948.2	0.018282	2.6×10^{-5}	0.018267	1.5×10^{-5}	0.018252	3.5×10^{-5}	590194	WISEA J084056.86+443127.4	0.089493	1.3×10^{-5}	0.089513	2.0×10^{-5}	0.089532	1.3×10^{-5}	2011im	NGC 7364	0.016161	0.6×10^{-5}	0.016163	0.2×10^{-5}	0.016164	0.8×10^{-5}	2013gs	UGC 5066	0.016797	1.6×10^{-5}	0.016812	1.5×10^{-5}	0.016827	1.7×10^{-5}																																						
2010A	UGC 2019	0.020745	1.2×10^{-5}	0.020755	1.0×10^{-5}																																																																																						
		0.020765	1.4×10^{-5}			2010ag	UGC 10679	0.033690	1.1×10^{-5}	0.033715	2.5×10^{-5}	0.033739	1.2×10^{-5}	2010ai	WISEA J125925.01+275948.2	0.018282	2.6×10^{-5}	0.018267	1.5×10^{-5}	0.018252	3.5×10^{-5}	590194	WISEA J084056.86+443127.4	0.089493	1.3×10^{-5}	0.089513	2.0×10^{-5}	0.089532	1.3×10^{-5}	2011im	NGC 7364	0.016161	0.6×10^{-5}	0.016163	0.2×10^{-5}	0.016164	0.8×10^{-5}	2013gs	UGC 5066	0.016797	1.6×10^{-5}	0.016812	1.5×10^{-5}	0.016827	1.7×10^{-5}																																														
2010ag	UGC 10679	0.033690	1.1×10^{-5}	0.033715	2.5×10^{-5}																																																																																						
		0.033739	1.2×10^{-5}			2010ai	WISEA J125925.01+275948.2	0.018282	2.6×10^{-5}	0.018267	1.5×10^{-5}	0.018252	3.5×10^{-5}	590194	WISEA J084056.86+443127.4	0.089493	1.3×10^{-5}	0.089513	2.0×10^{-5}	0.089532	1.3×10^{-5}	2011im	NGC 7364	0.016161	0.6×10^{-5}	0.016163	0.2×10^{-5}	0.016164	0.8×10^{-5}	2013gs	UGC 5066	0.016797	1.6×10^{-5}	0.016812	1.5×10^{-5}	0.016827	1.7×10^{-5}																																																						
2010ai	WISEA J125925.01+275948.2	0.018282	2.6×10^{-5}	0.018267	1.5×10^{-5}																																																																																						
		0.018252	3.5×10^{-5}			590194	WISEA J084056.86+443127.4	0.089493	1.3×10^{-5}	0.089513	2.0×10^{-5}	0.089532	1.3×10^{-5}	2011im	NGC 7364	0.016161	0.6×10^{-5}	0.016163	0.2×10^{-5}	0.016164	0.8×10^{-5}	2013gs	UGC 5066	0.016797	1.6×10^{-5}	0.016812	1.5×10^{-5}	0.016827	1.7×10^{-5}																																																														
590194	WISEA J084056.86+443127.4	0.089493	1.3×10^{-5}	0.089513	2.0×10^{-5}																																																																																						
		0.089532	1.3×10^{-5}			2011im	NGC 7364	0.016161	0.6×10^{-5}	0.016163	0.2×10^{-5}	0.016164	0.8×10^{-5}	2013gs	UGC 5066	0.016797	1.6×10^{-5}	0.016812	1.5×10^{-5}	0.016827	1.7×10^{-5}																																																																						
2011im	NGC 7364	0.016161	0.6×10^{-5}	0.016163	0.2×10^{-5}																																																																																						
		0.016164	0.8×10^{-5}			2013gs	UGC 5066	0.016797	1.6×10^{-5}	0.016812	1.5×10^{-5}	0.016827	1.7×10^{-5}																																																																														
2013gs	UGC 5066	0.016797	1.6×10^{-5}	0.016812	1.5×10^{-5}																																																																																						
		0.016827	1.7×10^{-5}																																																																																								

Table A2. Heliocentric redshift update discrepancies $\geq 1 \times 10^{-3}$. Discrepancies that arise from SN redshifts are generally not included (unless they are particularly large or unusual) since they are routinely larger than 1×10^{-3} .

SNID	Host	z_{old}	z_{new}	Difference	Comments
2014bj	WISEA J192240.35+435317.7	0.005	0.043	3.8×10^{-2}	Original ATTEL adopts a redshift of 0.045 (Zhang & Wang, 2014), subsequent classification 0.043 (Balam, 2016), photometric host redshift of 0.042 (Yan et al., 2014) is in agreement. Old redshift comes from Stahl et al. (2019), which cites CBET 3893 (Yuk et al., 2014). The smaller redshift is a valid but less likely fit to the SN spectrum.
2009dc ^a	UGC 10064	0	0.021787	2.2×10^2	Only affects CSP DR2 redshift, and was corrected in DR3.
14782	SDSS J205656.18-001645.0	0.179	0.1604	-1.9×10^{-2}	New redshift is spectroscopic host redshift, and agrees with SNID redshift of 0.165 (Östman et al., 2011). Sako et al. (2018) publishes the old redshift 0.179, which is a SN redshift. We mention this particular example of SN to host redshift because it is an extreme outlier.
Strolger	...	1.01	1.027	1.7×10^{-2}	Uncertain origin of z_{old} ; z_{new} matches Riess et al. (2007).
580104	...	0.31	0.3232	1.3×10^{-2}	z_{old} comes from PS1MD but was measured to higher precision by DES (580104 is the same SN as 1261579).
Mcguire	...	1.37	1.357	-1.3×10^{-2}	Potential typo; z_{new} matches Riess et al. (2007).
2007co	CGCG 172-029	0.016962	0.026962	1.0×10^{-2}	Appears to be an error in the SOUSA record (leading 1 should be a 2). z_{new} confirmed by CfA3, LOSS records and classification CBET (Blondin et al., 2007).
2002hu	MCG +06-06-012	0.03	0.0367	6.7×10^{-3}	Origin of z_{old} appears to be the NED reference to IAUC 8013 (Matheson et al., 2002), that incorrectly states a redshift of 0.03. z_{new} is from Matheson et al. (2002), who state the recession velocity of the host galaxy is 11000 km s^{-1} , which translates to $z = 0.0367$.
2008ad	2MASS J12493690+2819445	0.050	0.055441	5.4×10^{-3}	Appears to be a NED error; classification CBET finds $z = 0.054$ (Yuan et al., 2008a) while NED reports $z_{old} = 0.05$ for the host name WISEA J124936.88+281944.7. z_{new} from SDSS DR13.
2010ai	WISEA J125925.01+275948.2	0.0233	0.018267	-5.0×10^{-3}	SN and host are part of a cluster, possibly resulting in $z_{old} = 0.0233$. Original CBET fits a redshift of 0.014 (Nakano et al., 2010), more or less consistent with SDSS DR13 measurement $z_{new} = 0.018267$ of nearest galaxy.
Lancaster	...	1.23	1.235	5.0×10^{-3}	Possible rounding error; z_{new} matches Riess et al. (2007).
2005lz	UGC 1666	0.039968	0.044341	4.4×10^{-3}	z_{new} from the 2MASS redshift survey (2MRS, Huchra et al., 2012). z_{old} appears to be the original SN z of 0.04 (Silverman et al., 2012; Blondin et al., 2012) circularly converted from z_{CMB} .
2007qe	WISEA J235412.07+272431.9	0.019977	0.02396	4.0×10^{-3}	z_{old} appears to be a circular conversion of the erroneous NED redshift $z = 0.02$ from Garnavich et al. (2007), who actually quote 0.024. This is consistent with the z_{new} we take from Childress et al. (2013) who perform dedicated host spectroscopy.
2007mm ^a	WISEA J010546.37-004533.6	0.068921	0.065349	-3.6×10^{-3}	z_{new} comes from SDSS DR13 while z_{old} is the approximate heliocentric correction to the original CBET $z = 0.07$ (Bassett et al., 2007).
2006cz	MCG-01-38-002	0.03833	0.0418	3.5×10^{-3}	Origin of z_{old} uncertain. z_{new} from 2dFGRS (Colless et al., 2003).
2007ci	NGC 3873	0.021275	0.017954	-3.3×10^{-3}	Origin of z_{old} uncertain, as it appears to be closer to the average of the two nearest galaxies. We take the SDSS DR 13 redshift of the the nearest galaxy, the most likely host.
1997dg	WISEA J234014.14+261209.8	0.033960	0.03081	-3.2×10^{-3}	z_{old} is a circular conversion of the original SN redshift estimation of 0.034 from IAUC 6753 (Wang et al., 1997), whereas z_{new} is from host spectroscopy (Jha et al., 2006).
Yowie	...	0.46	0.457	-3.0×10^{-3}	Potential rounding; z_{new} matches Riess et al. (2007).
2005M	NGC 2930	0.0220	0.02484	2.8×10^{-3}	z_{old} from the Catalogue of Optical Radial Velocities (CORV, Fouqué et al., 1992), while z_{new} is from Childress et al. (2013).
2005al	NGC 5304	0.015202	0.0124	-2.8×10^{-3}	Only affects CSP DR2 record; CSP DR3 redshift agrees with z_{new} from Childress et al. (2013).
PTF09dnp	WISEA J151925.36+493004.8	0.04	0.037304	2.7×10^{-3}	Origin of z_{old} is unclear as the value of 0.04 only seems to appear in SOUSA, at https://archive.stsci.edu/prepds/sousa/ . z_{new} is from SDSS DR13.
1999ej	NGC 495	0.016388	0.013723	-2.7×10^{-3}	Origin of z_{old} uncertain, z_{new} from the Third Reference Catalogue of Bright Galaxies (RC3, de Vaucouleurs et al., 1991) (which was used in the original CfA2 publication (Jha et al., 2006)).
2006oa	WISEA J212342.91-005034.7	0.059936	0.062573	2.6×10^{-3}	z_{new} is from the SDSS II SN Survey data release (Sako et al., 2018). z_{old} appears to be the original SN z of 0.06 (Bassett et al., 2006) circularly converted from z_{CMB} .
2007cv	IC 2597	0.007562	0.009974	2.4×10^{-3}	z_{old} is from Bosma & Freeman (1993), which disagrees with all other measurements in NED. z_{new} from 6dF DR3 (Jones et al., 2009).

Table A2. (Continued)

SNID	Host	z_{old}	z_{new}	Difference	Comments
2017erp ^a	NGC 5861	0.0045	0.006904	2.4×10^{-3}	Only affects FSS record. Uncertain origin of z_{old} . z_{new} from 6dF DR3.
ASASSN-14lw	WISEA J010647.87-465901.4	0.023	0.0209	-2.1×10^{-3}	z_{old} is potentially the average redshift of the galaxy cluster around where ASASSN-14lw occurred according to ATEL 6809 (Kiyota et al., 2014). However, z_{new} is the spectroscopic host redshift measured by CSP-II (Phillips et al., 2019).
2007nq	UGC 595	0.043523	0.04521	1.7×10^{-3}	Origin of z_{old} uncertain, z_{new} from Childress et al. (2013).
1993ae	IC 126	0.017932	0.019667	1.7×10^{-3}	z_{old} appears to be a circular conversion of the z_{CMB} from Jha et al. (2007), while z_{new} is from 6dF DR3.
2008fr	LEDA 5069093	0.040656	0.039	-1.7×10^{-3}	z_{old} appears to come from the redshift 0.0407 quoted by SIMBAD, which is the least reliable SNID redshift from Silverman et al. (2012, Table 7). We take z_{new} to be the original CBET (Yuan et al., 2008b) which agrees with Silverman et al. (2012) Table 1.
2002fk	NGC 1309	0.0055856	0.007185	1.6×10^{-3}	Origin of z_{old} uncertain. z_{new} taken from 6dF DR3, and agrees with SN 2012Z also hosted by NGC 1309.
1999aa	NGC 2595	0.016019	0.014422	-1.6×10^{-3}	z_{old} appears to be a double heliocentric correction. z_{new} is from SDSS DR13.
2019np ^a	NGC 3254	0.004	0.005502	1.5×10^{-3}	Origin of z_{old} unclear. z_{new} comes from Springob et al. (2005).
2008L	NGC 1259	0.017845	0.01928	1.4×10^{-3}	z_{old} appears to be roughly the average redshift of the Perseus cluster. We take z_{new} to be that of the host galaxy only (Jørgensen et al., 2018).
2007ux	2MASX J10091969+1459268	0.029324	0.030699	1.4×10^{-3}	Origin of z_{old} uncertain, z_{new} from SDSS DR13.
2010cr	NGC 5177	0.022925	0.021551	-1.4×10^{-3}	Origin of z_{old} uncertain, z_{new} from SDSS DR13.
2015N	UGC 11797	0.013930	0.012499	-1.4×10^{-3}	z_{old} is from the Updated Zwicky Catalogue (UZC, Falco et al., 1999), while z_{new} is from 2MRS. The redshift of UGC 11797 is contentious, possibly due to interaction with UGC 11798.
PSNJ1628383	NGC 6166 ^b	0.031188	0.029831	-1.4×10^{-3}	z_{old} from FSS, but z_{new} is the average of the three nearest galaxies since a unique host cannot be determined (Figure 2).
2006bz	IC 4042A	0.0268	0.028115	1.3×10^{-3}	z_{old} from CORV while z_{new} comes from SDSS DR6.
2006kf	UGC 2829	0.0212992	0.020037	-1.3×10^{-3}	z_{new} from 21 cm H I emission (Springob et al., 2005). z_{old} appears to be original CfA Redshift Survey z of 0.021301 (Huchra et al., 1999) circularly converted from z_{CMB} .
2008fp	ESO 428-G014	0.006966	0.005664	-1.3×10^{-3}	Only affects CSP DR2 record; z_{old} appears to be a double heliocentric correction. z_{new} comes from host spectroscopy (Wegner et al., 2003), and is consistent with SN spectrum (Wang et al., 2008) and CSP DR3.
2004gc ^a	ARP 327 NED04	0.030715	0.03196	1.2×10^{-3}	Only affects CSP DR2 record. Origin of z_{old} uncertain. z_{new} from Childress et al. (2013) and consistent with CSP DR3.
2006qo	UGC 4133	0.028521	0.029704	1.2×10^{-3}	Origin of z_{old} uncertain. z_{new} from 21 cm emission (Theureau et al., 1998).
1996C	MCG+08-25-047	0.027016	0.028235	1.2×10^{-3}	z_{old} appears to be a circular conversion of the original redshift (weak H α emission, Mueller et al., 1996), while z_{new} comes from SDSS DR13.
2006lu	WISEA J091517.24-253600.6	0.054458	0.0534	-1.1×10^{-3}	Only affects CSP DR2 record; z_{old} appears to be the CMB-frame redshift. z_{new} is from Folatelli et al. (2013), and is the same redshift quoted by CSP DR3.
2000B	NGC 2320	0.020196	0.019141	-1.1×10^{-3}	Origin of z_{old} uncertain, z_{new} from host spectroscopy (van den Bosch et al., 2015).
2012ht ^a	NGC 3447A	0.003599	0.004646	1.1×10^{-3}	This was a case of the heliocentric-frame redshift being used as the CMB-frame redshift. z_{new} comes from SDSS DR13.
2001fh	WISEA J212042.46+442359.3	0.0123	0.013303	1.0×10^{-3}	Origin of z_{old} uncertain. z_{new} from van den Bosch et al. (2015).
160099	WISEA J141838.64+541054.8	0.100	0.101018	1.0×10^{-3}	z_{new} is from SDSS DR 13.
2007cq	WISEA J221440.71+050442.3	0.025	0.02604	1.0×10^{-3}	Origin of z_{old} (SQUAS record) uncertain as it does not match the classification CBET (Filippenko et al., 2007). z_{new} is from Childress et al. (2013).
2007aj	SDSS J124754.53+540038.5	0.031019	0.30	-1.0×10^{-3}	Origin of z_{old} uncertain, and has been replaced by the original SN z (Quimby et al., 2007).
Eagle	...	1.02	1.019	-1.0×10^{-3}	Potential rounding; z_{new} matches Riess et al. (2007).
Rakke	...	0.74	0.739	-1.0×10^{-3}	Potential rounding; z_{new} matches Riess et al. (2007).

^aMissing heliocentric redshift, so these cases are actually CMB-frame redshift discrepancies.^bThis host was assigned by FSS because it is the closest and largest of the three nearby galaxies but we do not attempt to pick a unique host (see Figure 2).

Table A3. Supernovae previously without redshift uncertainties. The uncertainty is assigned to be 5×10^{-3} if the redshift is measured directly from a SN spectrum without host emission, and 9×10^{-5} if not.

SNID	Host	z_{hel}	Assigned Uncertainty
1992J	WISEA J100901.19-263836.3	0.0446	9×10^{-5}
1992ae	WISEA J212817.17-613302.7	0.0752	9×10^{-5}
1992aq	APMUKS(BJ) B230147.96-373644.6	0.101	9×10^{-5}
1993B	WISEA J103451.50-342635.8	0.0696	9×10^{-5}
1993ac	CGCG 307-023	0.04937	9×10^{-5}
1995bd	UGC 03151	0.01539	9×10^{-5}
1996bl	WISEA J003618.14+112335.3	0.036	9×10^{-5}
2001az	UGC 10483	0.040695	9×10^{-5}
2002hu ^a	MCG +06-06-012	0.0367	1.0×10^{-3}
2002kf	CGCG 233-023	0.01930	9×10^{-5}
2003hu	2MASX J19113272+7753382	0.075	9×10^{-5}
2006an	SDSS J121438.73+121347.7	0.064	9×10^{-5}
2006is	WISEA J051734.55-234659.7	0.0314	9×10^{-5}
2006lu	WISEA J091517.24-253600.6	0.0534	9×10^{-5}
2006td	KUG 0155+361	0.015881	9×10^{-5}
2008L	NGC 1259	0.01928	9×10^{-5}
2008by	WISEA J120520.83+405645.9	0.045	9×10^{-5}
2008cf	LEDA 766647	0.04603	9×10^{-5}
2008fk	WISEA J023405.17+012340.2	0.072	9×10^{-5}
2008gb	UGC 02427	0.037	9×10^{-5}
ASASSN-16es	SDSS J115054.45+021828.1	0.02850 ^b	9×10^{-5}
ASASSN-16hh	MCG +03-06-031	0.03026 ^b	9×10^{-5}
ASASSN-16lc	WISEA J192901.71-515812.6	0.02033 ^b	9×10^{-5}
2017gup	WISEA J032934.19+105825.5	0.02316 ^b	9×10^{-5}
2017hoq	WISEA J051920.10-173647.6	0.02341 ^b	9×10^{-5}
2018enc	WISEA J151928.86-095256.6	0.02389 ^b	9×10^{-5}
2018fop	WISEA J011517.81-065130.5	0.02121 ^b	9×10^{-5}
2018jjd	GALEXASC J042420.17-315913.5	0.02560 ^b	9×10^{-5}
ASASSN-18da	WISEA J032916.56-235839.3	0.02200 ^b	9×10^{-5}
ASASSN-18iu	WISEA J175740.54+500200.6	0.02230 ^b	9×10^{-5}
1996ab	Anonymous	0.123	5×10^{-3}
2006mp	UGC 10754 NOTES01	0.023	5×10^{-3}
2007aj	SDSS J124754.53+540038.5	0.030	5×10^{-3}
2007kf	WISEA J173130.93+691844.3	0.0467	5×10^{-3}
2007kg	Anonymous	0.0067	5×10^{-3}
2007kh	SDSS J031512.10+431012.9	0.050	5×10^{-3}
2010hs	WISEA J022537.66+244557.17	0.076	5×10^{-3}
LSQ13crf	WISEA J031050.33+012519.7	0.060	5×10^{-3}
2014bj	WISEA J192240.35+435317.7	0.043	5×10^{-3}
2017dws	WISEA J154014.24+112040.8	0.082	5×10^{-3}
2017hbi	WISEA J023232.07+352854.8	0.040	5×10^{-3}

^a2002hu is the only exception, which is a host redshift we have inflated the uncertainty on due to particularly ambiguous reporting of redshifts.

^bRedshift independently measured by Chen *et al.* (2020), but redshift uncertainties have not been released at the time of writing.

Appendix B. Converting real-space velocities to redshift-space velocities

Here we detail how we transfer the 2M++ velocity reconstruction from real space to redshift space. The purpose of this transformation is so that we do not need to convert redshifts to distances in order to estimate their peculiar velocities.

B.1 Scaling the 2M++ real-space grid

As in Equation (9), the peculiar velocity grid must be scaled from the normalised reconstruction to best match observed peculiar velocities from the Tully-Fisher and Fundamental Plane relations. Each real-space grid point is scaled by β and adjusted by \mathbf{V}_{ext} :

$$\mathbf{v}_p = \beta \mathbf{v}_{p,\text{recon.}} + \mathbf{V}_{\text{ext}}, \tag{B1}$$

where $\mathbf{v}_p = (v_x, v_y, v_z)$ are the new scaled velocities at real-space grid points $\mathbf{r} = (X, Y, Z)$. The projected line of sight velocity for each grid point is

$$v_{\text{proj.}} = \mathbf{v}_p \cdot \hat{\mathbf{r}} \tag{B2}$$

B.2 Converting to supergalactic coordinates in real-space

The 2M++ real-space grid is in galactic Cartesian coordinates, so we transform to supergalactic Cartesian coordinates by rotating via

$$R = \begin{pmatrix} -\sin(l) & \cos(l) & 0 \\ -\sin(b)\cos(l) - \sin(b)\sin(l) & \cos(b) & \\ \cos(b)\cos(l) & \cos(b)\sin(l) & -\sin(b) \end{pmatrix}, \tag{B3}$$

so that the positive z-direction (now SGZ) is in the direction of the supergalactic north pole, $(l, b) = (47.37^\circ, 6.32^\circ)$ (Lahav et al. 2000). With $\mathbf{r}_{\text{SG}} = (\text{SGX}, \text{SGY}, \text{SGZ})$ and $\mathbf{v}_{\text{SG}} = (v_{\text{SGX}}, v_{\text{SGY}}, v_{\text{SGZ}})$,

$$\mathbf{r}_{\text{SG}}^T = R\mathbf{r}^T, \tag{B4}$$

and

$$\mathbf{v}_{\text{SG}}^T = R\mathbf{v}_p^T. \tag{B5}$$

The projected line of sight velocity using supergalactic coordinates in real-space is

$$v_{\text{SG,proj.}} = \mathbf{v}_{\text{SG}} \cdot \hat{\mathbf{r}}_{\text{SG}} \tag{B6}$$

B.3 Converting to redshift-space

The distance to any grid point is

$$D = \sqrt{\mathbf{r} \cdot \mathbf{r}} = \sqrt{\mathbf{r}_{\text{SG}} \cdot \mathbf{r}_{\text{SG}}} = \sqrt{\text{SGX}^2 + \text{SGY}^2 + \text{SGZ}^2}. \tag{B7}$$

We then adjust the redshift of each grid point by its associated peculiar redshift via

$$z = [(1 + \bar{z})(1 + z_p) - 1], \tag{B8}$$

where \bar{z} is the cosmological redshift corresponding to D in $h^{-1}\text{Mpc}$ using $H_0 = 100h \text{ km s}^{-1}\text{Mpc}^{-1}$ (making it independent of H_0), $\Omega_m = 0.3$ (the same value used in the reconstruction process), and $z_p \approx v_{\text{SG,proj.}}/c$. The redshift-space position vector is then the real-space position vector converted to redshift by the ratio of z to D ,

$$\mathbf{z} = \frac{z}{D} \mathbf{r}_{\text{SG}}. \tag{B9}$$

However, the grid points are now irregularly spaced. Thus, the final step is to use inverse distance weighting to interpolate and adjust the irregularly-spaced grid to a regular grid.